A study on time discretization and adaptive mesh refinement methods for the simulation of cancer invasion: the urokinase model.

Niklas Kolbe *, Jana Kat'uchová †, Nikolaos Sfakianakis ‡, Nadja Hellmann §, and

Mária Lukáčová-Medviďová ¶

Wednesday 17th June, 2015

Abstract

In the present work we investigate a model that describes the chemotactically and proteolytically driven tissue invasion by cancer cells. The model is a system of advection-reaction-diffusion equations that takes into account the role of the serine protease urokinase-type plasminogen activator. The analytical and numerical study of such a system constitutes a challenge due to the merging, emerging, and travelling concentrations that the solutions exhibit.

Classical numerical methods applied to this system necessitate very fine discretization grids to resolve these dynamics in an accurate way. To reduce the computational cost without sacrificing the accuracy of the solution, we apply adaptive mesh refinement techniques, in particular h-refinement. Extended numerical experiments show that this approach provides with a higher order, stable, and robust numerical method for this system. We elaborate on several mesh refinement criteria and compare the results with the ones in the literature.

We prove, for a simpler version of this model, L^∞ bounds for the solutions. We also studied the stability of its conditional steady states, and conclude that it can serve as a test case for further development of mesh refinement techniques for cancer invasion simulations.

Key words: cancer modelling, chemotaxis, merging and emerging concentrations, finite volume method, IMEX, adaptive mesh refinement

AMS subject classification: 92B05, 35Q92, 65M08, 65M50

1 Introduction

Cancer is one of the most frequent causes of death worldwide. By 2020 about 70% of all cancer-related death will occur in developing countries, due to a survival rate of only about 20%-30% due to a late diagnosis, [47]. The development of cancer involves different sub-processes like growth, vascularization, tissue invasion, and metastasis, [22].

Cancer research aims to understand the causes of cancer and to develop strategies for its diagnosis and treatment. The overall effort is highly interdisciplinary, involving components from medical science, biology, chemistry, physics, informatics, and mathematics. Mathematics in particular contributes in this research with the modelling of the biological processes, the corresponding analysis, and the numerical simulations of a wide range of processes spanning from intracellular bio-chemical reactions to cancer growth and metastasis.

*Institute of Mathematics, University of Mainz, Germany   kolbe@uni-mainz.de
†Faculty of Medicine, University of Košice, Slovakia   katuchova@gmail.com
‡Institute of Mathematics, University of Mainz, Germany   sfakiana@uni-mainz.de
§Institute of Molecular Biophysics, University of Mainz, Germany   nhellman@uni-mainz.de
¶Institute of Mathematics, University of Mainz, Germany   lukacova@uni-mainz.de

The growth and invasion of cancer has been the subject of many theoretical studies, concentrating on different aspects and employing different mathematical approaches, for example: cancer growth [1, 40, 7]; cancer cells invasion of the Extracellular Matrix (ECM) [38, 3, 50, 13, 15, 39, 46, 35]; cancer stem cell modelling [17, 45].

This is the first of a series of papers where we address models of invasion of cancer cells into the ECM. These papers involve the degeneration of the adjacent tissue by the cancer cells and their subsequent migration into nearby areas. We model, analyse, and numerically resolve different biological theories that address pathways of chemical interactions taking place during the invasion of the cancer cells.

In the current paper in particular, our objective is to lay the foundation and to propose/present the numerical treatment that we use in our studies. To this end, we focus on a model introduced by Chaplain and Lolas in [30, 8] and further analyzed in [2, 14, 15, 46, 26]. This model describes the dynamics of cancer invasion using deterministic descriptions of macroscopic quantities. The invasion process is dominated by directed cell movement due to the gradients of extracellular chemicals (chemotaxis) and the gradient in the structure of the ECM (haptotaxis). The model includes further the interactions of the cancer cells with extracellular proteins, a part of their chemical pathway, and their diffusion.

Due to the model dynamics, suitable, accurate numerical methods of high order are needed for the simulations. In the literature, various techniques have already been applied to this and similar models. These include among others Finite Differences combined with Backward Differentiation Formulas (BDF) in time (see e.g. [8]), and second order Finite Volume (FV) methods combined with linearly implicit time integration methods like the Rosenbrock-Wanner Multiple Arnoldi Process (ROWMAP) method (see e.g. [14, 2, 19]). Because of the computational challenge of this type of problems, and since we employ adaptive mesh refinement, we need to have a complete control of both the challenging dynamical behaviour of the mathematical model and problem-suited adaptive numerical schemes.

In a first step we compare several time integration techniques, some of which have been used for similar problems, employed with a FV method introduced in [28]. We notice that even in one-dimensional experiments that a (very) large number of grid cells (of the order of 10^3) is needed to properly resolve the dynamics, albeit the methods employed are stable and second order accurate. For smaller cell numbers large deviations in the propagation speed of the wave fronts occur, an indication that the numerical error depends heavily on the size of the computational cells and is of the magnitude of the model dynamics. The corresponding two-dimensional experiments exhibit similar behaviour; using though a grid as fine as in the one-dimensional case, renders the computation prohibitively expensive.

Such difficulties are not new in the mathematical literature; there are several examples where the convergence of a numerical method depends heavily on the size of the discretization cells, and at the same time, the use of uniformly fine discretization grids is not satisfactory due to the increased computational cost. In such cases, mesh refinement techniques are often seen as an alternative numerical treatment. With such methods, one alters the density of the discretization grid either by refining the mesh locally, or by complete mesh reconstruction. It has been seen, time and again, that such methods can improve the quality of the numerical solutions, and at the same time reduce the computational costs, see e.g. [5, 27, 31, 41, 43].

In the present paper we take the first step into obtaining efficient adaptive numerical techniques for the class of cancer invasion problems, in particular of *h-refinement* in the form of cell bisection based on properly chosen estimator functions.

Furthermore, we study analytically a reduced chemotaxis-haptotaxis model with logistic growth, and compare it with the original system in terms of qualitative behaviour of their respective solutions. We investigate the conditional stability of the steady states for particular parameter ranges and justify the similarities in the transient behaviour of merging, emerging and travelling concentrations that both systems exhibit. We prove L^∞ bounds, allowing hence to use the smaller model and the corresponding parameter set, as a test case for the development of further mesh refinement techniques for the cancer invasion models.

The rest of the paper is structured as follows: In Section 2 we describe shortly the relevant physiological aspects of tumor biology. We present in Section 3 the main mathematical model of tumor proliferation and invasion that we use in this work. In Section 4 we present two reduced models that exhibit the same

dynamics as the main model, study their stability and prove appropriate L^∞ bounds. In Sections 5 and 6 we describe the numerical methods, and the mesh refinement techniques which we use and present and discuss the results of several numerical experiments.

2 Tumor Biology

Tumorgenesis is a multistep process, in which normal cells progressively convert to cancer cells. This process is associated with various changes in cell physiology common to most of the cancers. These are, in particular, self-sufficiency in growth signals, insensitivity to inhibitory growth signals, evasion of programmed cell death, limitless replicative potential, sustained angiogenesis, tissue invasion and metastasis, and immunoediting [20, 34, 47, 11].

Tumor development is directly and indirectly influenced by paracrine as well as autocrine signals. Such factors include angiogenesis factors, growth factors, chemokines (signaling molecules originally characterized by their ability to induce chemotaxis), cytokines, hormones, enzymes, cytolytic factors, and so forth, which may promote or reduce tumor growth [47]. One important property which distinguishes tumor cells from normal cells is their ability to proliferate infinitely. This is the result of changes in cell death signaling pathways (apoptosis)[24]. Angiogenesis is a further important factor for tumor growth. Growth of blood capillaries into the tumor is necessary for supply of nutrient and oxygen, and is induced by growth factors, such as Vascular Endothelial Growth Factor (VEGF). Angiogenesis is also required for metastases and tissue invasion of the tumor. Metastatic tumors are the cause of about 90% of human cancer deaths [44]. Spreading of metastases is possible through hematogenous and lymphogeneous pathways, which guide the metastases to other locations in the body, where they settle. Both intravasation and extravasation (entering / exiting capillaries or lymphatic vessels) is characterized by changes in the ECM surrounding the tumor and its interactions with tumor cells.

Molecular analysis indicates the importance of chemotactic motion in understanding of the outgrowth of tumor cells. Meanwhile the importance of chemokines in tumor progression is acknowledged [54] e.g, for breast cancer cells that typically metastasizes in bone marrow, liver, lymph nodes and lung. These organs were found to secrete CXCL12, the ligand for the chemokine receptor CXCR4, which is enriched on breast cancer cells but not in normal breast epithelial cells [54].

Chemokines are now known to affect many aspects of tumor development such as angiogenesis and expression of cytokines, adhesion molecules, and proteases, and support of cancer cell migration. Thus chemotaxis plays an essential role in the successful outgrowth of tumors to the preferential organs.

Another important chemokine is the protein uPA (urokinase-plasminogen activator) and its inhibitor PAI-1 (plasminogen activator inhibitor 1). Both are part of the so-called urokinase plasminogen system which plays an essential role in the context of cancer progression and metastasis.

The protein uPA activates the protease plasmin, which is produced in an inactive form (plasminogen). Plasmin in turn produces the active form (uPA) by cleaving the inactive proform pro-uPA. This occurs mainly if pro-uPA is bound to its receptor uPAR; in solution the process is much less efficient. The resulting receptor bound uPA is the form which exhibits chemokine function, additionally it enhances the affinity of uPAR to vitronectin [52] and integrins. Vitronectin is a component of the ECM and responsible for the attachment of cells to ECM. It also binds to integrins which are transmembrane proteins and are responsible for signal transduction from the outside to the inside of the cell. This vitronectin-integrin interaction is indirectly regulated by the uPA/uPAR-complex, since the complex also interacts with integrins. Furthermore, the above mentioned PAI-1 inhibits the proteolytic function of uPA upon binding, both in the soluble and in the membrane-bound form, thus regulating the proteolytic network. The complex uPAR/uPA/PAI-1 is removed from the cell surface by endocytosis, triggering further signaling pathways related to cancer migration. PAI-1 also binds to vitronectin [42], and thus interferes with formation of cell-signaling and cell-ECM contacts.

Since intact ECM is a rather tight mesh composed of a number of different proteins, offering only small pores for the cell to move through, cleavage of ECM proteins by the cancer cells greatly enhances motility. The catalytic function of uPA, namely the activation of plasmin, is regarded as essential step in the

cancer-cell's ability to remodel the ECM. However, which ECM-components can be cleaved by plasmin *in vivo* is not well investigated, see [10], the best corrobated examples being laminin and fibronectin; however, MMPs which are activated by plasmin seem to have multiple roles in the regulation of tumor growth and progression (see [25] for an overview)

Thus, the proteins of this network, on one hand, help the tumor cell to remodel the ECM, so that it can detach from the original site and re-attach in another location; one the other hand, components of the network act as chemokines in order to guide the direction of tumor migration in this process. Below, we describe the most important aspects of the corresponding mathematical model as was introduced in [8].

3   Mathematical model

The primary model for cancer invasion that we investigate in this paper was first proposed in [8] and later studied in [2, 14, 15, 26, 46]. It focuses on the role of uPA and includes chemotactic/haptotactic driven motility, diffusion, and enzyme interactions. In following we give a short model derivation.

In this model, the cancer cells are represented by c, the ECM by the component vitronectin (VN) v, uPA, PAI-1, and plasmin by u, p, and m, and uPAR via the cancer cell density c. The differential equations for the different components are described shortly below; refer to [8] for further details.

Cancer cells. The spatio- temporal behavior of the cancer cells c is assumed to be determined by cellular diffusion, chemo- and haptotaxis due to uPA, PAI-1, and ECM gradients, logistic uPA/uPAR-complex driven proliferation. In particular:

$$\partial_t c = D_c \triangle c - \text{div}\left(\chi_u c \nabla u + \chi_p c \nabla p + \chi_v \nabla v\right) + \mu_1 c \left(1 - \frac{c}{c_0}\right) + \phi_{1,3} \, cu. \tag{3.1}$$

Extracellular matrix. For the ECM v, no transport terms are included since it is a non-motile structure. It is assumed though that it is constantly reconstructed, degraded by plasmin, produced indirectly by the formation of uPA/PAI-1 complex, and neutralized by the PAI-1/VN interaction:

$$\partial_t v = \mu_2 v \left(1 - \frac{v}{v_0}\right) - \delta vm + \phi_{2,1} \, up - \phi_{2,2} \, vp. \tag{3.2}$$

Urokinase plasmin activator. The uPA component u is assumed to diffuse, to bind to uPAR receptors and PAI-1 inhibitors, and to be secreted by the cancer cells:

$$\partial_t u = D_u \triangle u - \phi_{3,3} \, cu - \phi_{3,1} \, pu + \alpha_3 c. \tag{3.3}$$

Plasminogen activator inhibitor. The PAI-1 p is assumed to diffuse, to bind to uPA and to VN, and to be produced indirectly by plasmin:

$$\partial_t p = D_p \triangle p - \phi_{4,1} \, pu - \phi_{4,2} \, pv + \alpha_4 m. \tag{3.4}$$

Plasmin. The enzyme plasmin m is assumed to diffuse, to be activated by the uPA/uPAR complexes, and suppressed by the uPA/PAI-1 complexes, to be produced indirectly by the PAI-1/VN complex formation, and to degrade in time:

$$\partial_t m = D_m \triangle m + \phi_{5,3} \, uc - \phi_{5,1} \, pu + \phi_{5,2} \, pv - \alpha_5 m. \tag{3.5}$$

The model is formulated in non-dimensional variables by scaling with a reference length $L = 0.1$ cm, a reference diffusion coefficient $D = 10^{-6}$ cm^{2}s^{-1}, a rescaled time parameter $t = L^2 D^{-1}$, and reference

densities C, V, U, P, M for the cancer cells, vitronectin, uPA, PAI-1 and plasmin respectively. Keeping the former notations, the rescaled systems reads as follows:

$$
\begin{cases}
\partial_t c = D_c \Delta c & - \operatorname{div}(\chi_u c \nabla u + \chi_p c \nabla p + \chi_v c \nabla v) + \phi_{1,3} c u + \mu_1 c(1-c), \\
\partial_t v = & -\delta v m + \phi_{2,1} u p - \phi_{2,2} v p + \mu_2 v(1-v), \\
\partial_t u = D_u \Delta u & -\phi_{3,1} p u - \phi_{3,3} c u + \alpha_3 c, \\
\partial_t p = D_p \Delta p & -\phi_{4,1} p u - \phi_{4,2} p v + \alpha_4 m, \\
\partial_t m = D_m \Delta m & -\phi_{5,1} p u + \phi_{5,2} p v + \phi_{53} u c - \alpha_5 m.
\end{cases}
\tag{3.6}
$$

or, in vectorial form, as

$$
\mathbf{w}_t + A(\mathbf{w}) = D(\mathbf{w}) + R(\mathbf{w}).
\tag{3.7}
$$

where $\mathbf{w} = (c,\ v,\ u,\ p,\ m)^T$, $A(\mathbf{w}) = (\operatorname{div}(\chi_u c \nabla u + \chi_p c \nabla p + \chi_v c \nabla v),\ 0,\ 0,\ 0,\ 0)^T$,

$$
R(\mathbf{w}) =
\begin{pmatrix}
\phi_{13} c u + \mu_1 c(1-c) \\
-\delta v m + \phi_{21} u p - \phi_{22} v p + \mu_2 v(1-v) \\
-\phi_{31} p u - \phi_{33} c u + \alpha_3 c \\
-\phi_{41} p u - \phi_{42} p v + \alpha_4 m \\
-\phi_{51} p u + \phi_{52} p v + \phi_{53} u c - \alpha_5 m
\end{pmatrix}, \quad
D(\mathbf{w}) =
\begin{pmatrix}
D_c \Delta c \\
0 \\
D_u \Delta u \\
D_p \Delta p \\
D_m \Delta m
\end{pmatrix},
\tag{3.8}
$$

represent the vectors of variables, advection, reaction, and diffusion respectively. We note that the vectors for advection and diffusion include also derivatives of $\mathbf{w}$, which we have omitted in the notation for brevity.

The parameter set $\mathcal{P}$ we consider in this work is given by

$$
\begin{cases}
D_c = 3.5 \times 10^{-4}, & \chi_u = 3.05 \times 10^{-2}, & \mu_1 = 0.25, & \alpha_3 = 0.215, \\
D_u = 2.5 \times 10^{-3}, & \chi_p = 3.75 \times 10^{-2}, & \mu_2 = 0.15, & \alpha_4 = 0.5, \\
D_p = 3.5 \times 10^{-3}, & \chi_v = 2.85 \times 10^{-2}, & \delta = 8.15, & \alpha_5 = 0.5, \\
D_m = 4.91 \times 10^{-3}, & \phi_{13} = 0, & \phi_{21} = 0.75, & \phi_{22} = 0.55, \\
\phi_{31} = 0.75, & \phi_{33} = 0.3, & \phi_{41} = 0.75, & \phi_{42} = 0.55, \\
\phi_{51} = 0, & \phi_{52} = 0.11, & \phi_{53} = 0.75,
\end{cases}
\tag{3.9}
$$

These parameters have been estimated previously in the literature, see [2, 8, 30] for details.

4 Analytical properties of a chemotaxis-haptotaxis model with logistic source

Solutions of the system (3.6) feature heterogeneous spatio-temporal dynamics in the form of merging, emerging and travelling concentrations, see e.g. Figure 6.1.

It was in [2] that these dynamics result from the destabilization of single steady states of the system $\mathbf{w}_t = R(\mathbf{w})$ by advection. The nature of these dynamics and the size of the system (3.6) necessitate considerable computational effort, especially for the development of new numerical methods. To alleviate this burden we employ two simplified "versions" of (3.6) –systems (4.2) and (4.4)-(4.5) below– that are of the same nature, and whose solutions exhibit similar dynamical behavior as (3.6). We have used these reduced models to develop the numerical methods presented in this paper. Hence it is deemed necessary to address them (at least partially) and to describe their relation to the system (3.6).

The first simplified system, (4.2), was identified in the literature (e.g. [19], [36]) as the large time asymptotic limit of (3.6). For this system, we employed steady state analysis and identified a wide range of Fourier modes with positive amplification factors; in effect, small perturbations of the steady states

increase with time. In the numerical Section 6.3, we address the dynamics of the solution of this system, and note their similarities to the solutions of the system (3.6).

The second system, (4.4), is a regularized version of (4.2). The benefit of this system is that the increase of the perturbations of the steady states will not result in a blow-up of the solution (see Theorem 4.1), while the system maintains the dynamics of (4.2). This result is not only interesting in its own right, but is also fundamental for the development of stable mesh refinement methods. This is so, since the adaptive mesh refinement methods necessitate (as every numerical method) a minimum degree of smoothness of the solution. A blow-up in finite time, as is possible in bacterial chemotaxis models, would render any simulations after the blow-up time meaningless.

In order to analyse the linear stability of the simplified system (4.2), we assume that there exist a stable and spatially uniform steady state solution $\hat{\mathbf{w}} \in \mathbb{R}^d$ of a general system of the form $\mathbf{w}_t + A(\mathbf{w}) = R(\mathbf{w}) + D(\mathbf{w})$ on a periodic domain. As spatially uniform, $\hat{\mathbf{w}}$ is also a steady state of the reaction system $\mathbf{w}_t = R(\mathbf{w})$. If we neglect terms in $\mathcal{O}(\varepsilon^2)$, a small perturbation $\mathbf{w} = \hat{\mathbf{w}} + \varepsilon \mathbf{F_k}$ by a Fourier mode $\mathbf{F_k}$ with corresponding wave number k, grows in time, as long as the amplification factor

$$\lambda_k(\hat{\mathbf{w}}) = \max \left\{ \text{Real} \left\{ \text{spec} \left(J_R(\hat{\mathbf{w}}) - k^2 J_T(\hat{\mathbf{w}}) \right) \right\} \right\}, \tag{4.1}$$

is strictly positive, otherwise it is damped (cf. [2]). The matrices $J_R(\mathbf{w})$ and $J_T(\mathbf{w})$ denote the Jacobians of the reaction R and the general transport operator T such that $\text{div}\, T(\nabla \mathbf{w}) = D(\mathbf{w}) - A(\mathbf{w})$. In the case of the model (3.6) and parameter set $\mathcal{P}$, there is a spatially uniform steady state and a corresponding range of numbers k with $\lambda_k > 0$, which vanishes if chemo-, haptotaxis are neglected(i.e. if $\chi_u = \chi_p = \chi_v = 0$).

This process is now applied on the reduced system that is a chemotaxis model with logistic growth

$$\begin{cases} \partial_t c = D_c \Delta c - \nabla \cdot (\chi c \nabla u) + \mu c (1 - c), \\ \partial_t u = D_u \Delta u + \alpha c - \beta u. \end{cases} \tag{4.2}$$

In what follows, we demonstrate that small perturbations of the steady states of the reaction (sub-) system of (4.2) can increase due to positive amplification factors introduced if chemotaxis is included. In particular, f we neglect the transport terms in (4.2) we get a system of ordinary differential equations for $\mathbf{w} = (c, u)^T$ with steady state $\hat{\mathbf{w}} = (1, \frac{\alpha}{\beta})^T$, in which case, the Jacobians of reaction and generalized transport are given by

$$J_R(\mathbf{w}) = \begin{pmatrix} \mu(1 - 2c) & 0 \\ \alpha & -\beta \end{pmatrix}, \quad J_T(\mathbf{w}) = \begin{pmatrix} D_c & -\chi c \\ 0 & D_u \end{pmatrix}.$$

Choosing the parameters

$$D_c = 3.5 \times 10^{-4}, \quad D_u = 2.5 \times 10^{-3}, \quad \chi = 0.04, \quad \mu = 0.1, \quad \alpha = 0.115, \quad \beta = 0.4, \tag{4.3}$$

we obtain a range of wave numbers k with positive amplification factors $\lambda_k(\hat{\mathbf{w}})$, as shown in Figure 4.1. This implies that small perturbations of the steady states can increase in time. Indeed, as we see in Figure 4.1, chemotaxis (and not the diffusion) is responsible for the growth of perturbations, since the positive amplification factors vanish in the case $\chi = 0$. Analogous behaviour has been obtained for the system (3.6) in [2] and for (4.2) with $\alpha = \beta = 1$ in [36].

Clearly, a biologically reasonable requirement is that the solution does not blow-up. So, we need to show that it remains bounded in the L^∞ norm, despite the amplification –due to the taxis terms– of possible perturbations. To this end we employ the saturated chemotaxis flux introduced in [9, 28] and we modify system (4.2) as follows:

$$\begin{cases} \partial_t c = D_c \Delta c - \nabla \cdot (c\, Q(\chi \nabla u)) + \mu c (1 - c), \\ \partial_t u = D_u \Delta u + \alpha c - \beta u, \end{cases} \tag{4.4}$$
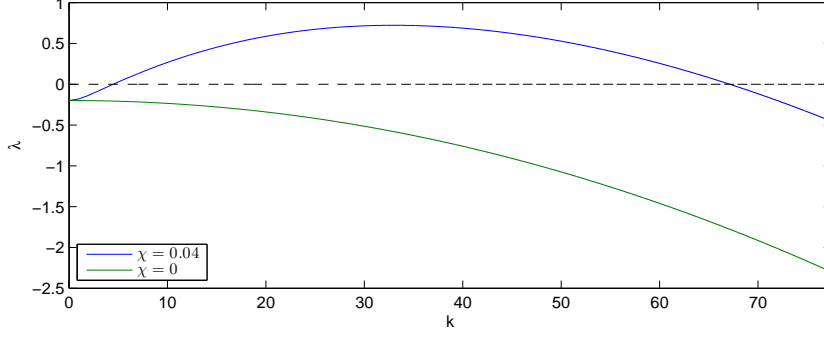
6

Figure 4.1: *A plot of $\lambda_k(\hat{\mathbf{w}})$ against k for the system (4.2) and the parameter set (4.3). The case with $\chi = 0.04$ exhibits positive amplifications factors for a wide range of modes; allowing hence for the increase of small perturbations of the steady states. When $\chi = 0$ all of the modes maintain negative amplification factors and the steady states of the corresponding reaction problem remain stable.*

where Q is given by

$$
Q(\chi\nabla u) = \begin{cases} \chi\nabla u, & \text{if } \chi|\nabla u| \leq S, \\ \left(\dfrac{\chi|\nabla u| - S}{\sqrt{1 + (\chi|\nabla u| - S)^2}} + S \right) \dfrac{\nabla u}{|\nabla u|}, & \text{otherwise,} \end{cases} \tag{4.5}
$$

for a positive constant S. The function Q limits the flux by $\|Q(\chi\nabla u)\| < S + 1 = C$.

Theorem 4.1. *We consider (4.4) on $\Omega \times [0, T)$, for a final time $0 < T < \infty$ and a compact set $\Omega \subset \mathbb{R}^d$ with a Lipschitz continuous boundary $\partial\Omega$ with the outer normal $\mathbf{n}$ and the boundary conditions*

$$
\frac{\partial c}{\partial \mathbf{n}} = \frac{\partial u}{\partial \mathbf{n}} = 0, \quad x \in \partial\Omega, \ t > 0. \tag{4.6}
$$

Let $(c(x,t), u(x,t))$ be a positive classical solution with bounded non-negative initial data. Then the following estimates hold,

$$
c(x,t) \leq \tilde{\tilde{C}} \max\left\{ \|c_o\|_{L^\infty(\Omega)}, \ \|c_0\|_{L^1(\Omega)} + \frac{T\mu|\Omega|}{4} \right\}, \tag{4.7}
$$

$$
u(x,t) \leq \|u_0\|_{L^\infty(\Omega)} + \frac{\tilde{\tilde{C}}\alpha}{\beta} \max\left\{ \|c_o\|_{L^\infty(\Omega)}, \ \|c_0\|_{L^1(\Omega)} + \frac{T\mu|\Omega|}{4} \right\}, \tag{4.8}
$$

for all $x \in \bar{\Omega}$ and $t \in [0, T]$, where

$$
\tilde{\tilde{C}} = \tilde{C} \left(1 + \frac{2D_c\mu}{C^2} \right)^2 \left(1 + \frac{\sqrt{C^2 + 2\mu D_c}}{D_c} \right)^{2d}, \tag{4.9}
$$

and $\tilde{C}$ depends on Ω only.

Proof. We follow [28] and multiply the first equation of (4.4) by c^{s-1} for $s \geq 2$. Integration by parts, the chain rule, the bound on Q as well as Young's inequality yield,

$$
\frac{1}{s}\frac{d}{dt}\int_\Omega c^s\, dx = -D_c \int_\Omega \nabla c \cdot \nabla(c^{s-1})\, dx + \int_\Omega c Q(\chi\nabla u) \cdot \nabla(c^{s-1})\, dx + \mu \int_\Omega c^s(1-c)\, dx
$$

$$
\leq -\frac{4D_c(s-1)}{s^2}\int_\Omega |\nabla(c^{\frac{s}{2}})|^2\, dx + \frac{2C(s-1)}{s}\int_\Omega c^{\frac{s}{2}}|\nabla(c^{\frac{s}{2}})|\, dx + \mu \int_\Omega c^s\, dx
$$

$$
\leq -\frac{4D_c(s-1)}{s^2}\|\nabla(c^{\frac{s}{2}})\|^2_{L^2(\Omega)} + \frac{2C(1-s)}{s}\int_\Omega \frac{1}{2}\left(\frac{2D_c}{Cs}|\nabla(c^{\frac{s}{2}})| + \frac{Cs}{2D_c}c^s \right)dx + \mu \int_\Omega c^s\, dx
$$

$$
\leq -\frac{2D_c(s-1)}{s^2}\|\nabla(c^{\frac{s}{2}})\|^2_{L^2(\Omega)} + \frac{C^2(s-1) + 2D_c\mu}{2D_c}\int_\Omega c^s\, dx.
$$

7

The last integral is estimated using the interpolation inequality,

$$\|\omega\|_{L^2(\Omega)}^2 \le \varepsilon\|\nabla\omega\|_{L^2(\Omega)}^2 + K(1+\varepsilon^{-\frac{d}{2}})\|\omega\|_{L^1(\Omega)}^2, \tag{4.10}$$

for a constant K depending only on the domain Ω and a chosen ε, [29]. We choose ε such that

$$\frac{C^2(s-1)+2D_c\mu}{2D_c} = \frac{2D_c(s-1)}{s^2\varepsilon} - \frac{C^2(s-1)+2D_c\mu}{2D_c} \Rightarrow \varepsilon = \frac{2D_c^2(s-1)}{C^2s^2(s-1)+2D_c\mu s^2} > 0,$$

and thus get

$$\frac{C^2(s-1)+2D_c\mu}{2D_c} \int_\Omega c^s\,dx = \left(\frac{2D_c(s-1)}{s^2\varepsilon} - \frac{C^2(s-1)+2D_c\mu}{2D_c}\right)\int_\Omega c^s\,dx$$

$$\le \frac{2D_c(s-1)}{s^2}\|\nabla(c^{\frac{s}{2}})\|_{L^2(\Omega)}^2 + \frac{2D_c(s-1)K(1+\varepsilon^{-\frac{d}{2}})}{s^2\varepsilon}\|c^{\frac{s}{2}}\|_{L^1(\Omega)}^2$$

$$- \frac{C^2(s-1)+2D_c\mu}{2D_c}\int_\Omega c^s\,dx.$$

Hence the dependence on $\nabla(c^{\frac{s}{2}})$ in the above estimates vanishes and using $\varepsilon^{-\frac{1}{2}} \le s\sqrt{C^2+2\mu D_c}/D_c$, we get

$$\frac{d}{dt}\int_\Omega c^s\,dx + \frac{sC^2(s-1)+2sD_c\mu}{2D_c}\int_\Omega c^s\,dx \le \frac{Ks\left(1+\left(\frac{s\sqrt{C^2+2\mu D_c}}{D_c}\right)^d\right)(C^2(s-1)+2D_c\mu)}{D_c}\left(\int_\Omega c^{\frac{s}{2}}\,dx\right)^2.$$

Next, we multiply by the integrating factor $e^{\kappa t}$, $\kappa = (sC^2(s-1)+2sD_c\mu)/2D_c$, and obtain after integrating over $[0,t]$, $0 < t \le T$ and eliminating the integrating factor

$$\int_\Omega c^s(x,t)\,dx \le \int_\Omega c_0^s\,dx + 2K\left(1+\frac{2D_c\mu}{C^2(s-1)}\right)\left(1+\frac{s\sqrt{C^2+2\mu D_c}}{D_c}\right)^d \sup_{0\le t\le T}\left(\int_\Omega c^{\frac{s}{2}}\,dx\right)^2 \tag{4.11}$$

Now, the function $M(s) = \max\left\{\|c_0\|_{L^\infty(\Omega)}, \sup_{0\le t\le T}\left(\int_\Omega c^{\frac{s}{2}}\,dx\right)^{\frac{1}{s}}\right\}$ satisfies the inequality

$$M(s) \le \left(\tilde{K}\left(1+\frac{2D_c\mu}{C^2(s-1)}\right)\left(1+\frac{s\sqrt{C^2+2\mu D_c}}{D_c}\right)^d\right)^{\frac{1}{s}} M\left(\frac{s}{2}\right).$$

Choosing the sequence $s = 2^k$, $k \in \mathbb{N}$, and dissolving the recursion by estimating the value of the monotonically increasing infinite product $\prod_{k=1}^\infty \left(1+2^kC\right)^{\frac{d}{2^k}} \le (2+2C)^{2d}$, we get

$$M(2^k) \le \tilde{C}\left(1+\frac{2D_c\mu}{C^2}\right)^2\left(1+\frac{\sqrt{C^2+2\mu D_c}}{D_c}\right)^{2d} M(1),$$

where $\tilde{C} = 2\max\{\tilde{K}, \tilde{K}^2\}$ depends on Ω only. Taking the limit $k \to \infty$, we end up with

$$\|c(\cdot,t)\|_{L^\infty(\Omega)} \le \tilde{C}\left(1+\frac{2D_c\mu}{C^2}\right)^2\left(1+\frac{\sqrt{C^2+2\mu D_c}}{D_c}\right)^{2d} M(1) = \tilde{\tilde{C}}M(1). \tag{4.12}$$

We further consider the mass of the component c by integrating the the first equation of (4.4) and obtain applying Gauss's theorem and using the non-negativity of c,

$$\frac{d}{dt}\int_\Omega c\,dx = \mu\int_\Omega c(1-c)\,dx \le \mu\int_\Omega \frac{1}{4}\,dx = \frac{\mu|\Omega|}{4},$$

since $c(1-c) \leq 1/4$ for any $c \geq 0$. Therefore we have

$$M(1) = \max\left\{\|c_o\|_{L^\infty(\Omega)}, \ \|c_0\|_{L^1(\Omega)} + \frac{T\,\mu|\Omega|}{4}\right\}.$$

Together with (4.12) the estimation for c follows.

Because of the maximum principle of heat equation, the solution of the following initial value problem,

$$\begin{cases} \dfrac{d\omega}{dt} = -\beta\omega + \alpha\tilde{\tilde{C}}M(1), \\ \omega(0) = \|u_0\|_{L^\infty(\Omega)}, \end{cases}$$

is an upper bound for u. Hence we can estimate

$$0 \leq u(x,t) \leq \omega(t) = e^{-\beta t}\|u_0\|_{L^\infty(\Omega)} + (1-e^{-\beta t})\frac{\alpha\tilde{\tilde{C}}}{\beta}M(1) \leq e^{-\beta t}\|u_0\|_{L^\infty(\Omega)} + \frac{\alpha\tilde{\tilde{C}}}{\beta}M(1),$$

which proves the $L^\infty(\Omega)$ bound of the density u. $\qquad\square$

Further analytical results regarding systems of the type (3.6), (4.2) include existence, uniqueness, and non-negativity of a classical solution for system (4.2) with homogeneous Neumann boundary conditions and non-negative initial data $c_0, \ u_0 \geq 0$, see e.g. [53, 48]. In [32] another simplified cancer invasion model that features also the degradation of the ECM was studied. By using particular change of variables and comparison principles the existence, uniqueness, positivity, and boundedness of the solutions was provided. In the more recent work [49], in the case of a quasi-steady-state ECM remodelling, existence, uniqueness, and boundedness of the solutions was proven.

5 Numerical Methods

The numerical methods studied in this paper are employed in both one- and two-dimensional domains (see also Section 6.5). To ease though the presentation we restrict ourselves, for the rest of the current section, to the one-dimensional case where the interval domain $\Omega = (a,b)$ is subdivided into a finite number of non overlapping, complementary computational cells

$$\Omega = \bigcup_{i=1}^{N} C_i,$$

with cell interfaces

$$a = x_{1/2}, \quad x_{i+1/2} = x_{i-1/2} + h_i, \ i = 1, \ldots, N-1, \quad x_{N+1/2} = b,$$

and sizes $|C_i| = h_i > 0$ satisfying $\sum_{i=1}^{N} h_i = b - a$. Correspondingly the cells and their centers reads as:

$$C_i = [x_{i-1/2}, x_{i+1/2}), \quad x_i = \frac{x_{i+1/2} + x_{i-1/2}}{2}, \quad i = 1, \ldots N.$$

In the paragraphs that follow, we present the space and time discretizations, as well as the mesh adaptivity method directly to the case of the system (3.6), although they can also be employed for the systems (4.2) and (4.4)-(4.5).

Space discretization. We discretize the system (3.6) with a FV method, and approximate a solution with piecewise constant functions

$$\mathbf{w}_i(t) \approx \frac{1}{|C_i|} \int_{C_i} \mathbf{w}(x,t) \ dx, \tag{5.1}$$

on every cell. In the following we present the discretization of the advection, reaction, and diffusion operators,

$$\mathcal{D}_i(\mathbf{w}_h(t)) \approx \frac{1}{|C_i|} \int_{C_i} D(\mathbf{w}(x,t)) \, dx, \qquad \mathcal{A}_i(\mathbf{w}_h(t)) \approx \frac{-1}{|C_i|} \int_{C_i} A(\mathbf{w}(x,t)) \, dx,$$

$$\mathcal{R}_i(\mathbf{w}_h(t)) \approx \frac{1}{|C_i|} \int_{C_i} R(\mathbf{w}(x,t)) \, dx,$$

where $\mathbf{w}_h(\cdot) = \{\mathbf{w}_i(\cdot)\}_{i=1}^{N}$. We discretize the reaction term by evaluating the reaction operator

$$\mathcal{R}_i(\mathbf{w}_h(t)) = R(\mathbf{w}_i(t)).$$

Concerning the diffusion, we use second order three-point central differences when the grid is uniform and second order five point central differences when the grid is non-uniform. In the latter case the discretization of the diffusion operator reads

$$\mathcal{D}_i(\mathbf{w}_h(t)) = D\left(\alpha_i^{(-2)}\mathbf{w}_{i-2}(t) + \alpha_i^{(-1)}\mathbf{w}_{i-1}(t) + \alpha_i^{(0)}\mathbf{w}_i(t) + \alpha_i^{(+1)}\mathbf{w}_{i+1}(t) + \alpha_i^{(+2)}\mathbf{w}_{i+2}(t)\right), \quad (5.2)$$

where D is a diagonal matrix with the vector $\begin{pmatrix} D_c & 0 & D_u & D_p & D_m \end{pmatrix}$ on the diagonal, and the co-efficients $\alpha_i^{(-2)}, \ldots, \alpha_i^{(+2)}$, σ_i, are chosen such that we get a second order approximation of the second derivative, i.e.

$$\alpha_i^{(-2)} = -8\frac{(h_{i-1} - h_{i+1})}{(h_{i-2} + 2h_{i-1} + 2h_i + 2h_{i+1} + h_{i+2})\sigma_i},$$

$$\alpha_i^{(-1)} = 8\frac{h_{i-1}(4h_{i-1} + 4h_{i-2} + 2h_i - 4h_{i+1} - 2h_{i+2}) + 3h_{i+1}^2}{(h_i + h_{i-1})(h_{i-1} + 2h_i + h_{i+1})\sigma_i}$$

$$+ 8\frac{h_{i+2}^2 + 4h_{i+1}h_{i+2} + h_i h_{i+2} + h_{i-2}(h_{i-2} - 2h_{i+1} - h_{i+2} + h_i)}{(h_i + h_{i-1})(h_{i-1} + 2h_i + h_{i+1})\sigma_i},$$

$$\alpha_i^{(+1)} = 8\frac{h_{i+1}(4h_{i+1} + 4h_{i+2} + 2h_i - 4h_{i-1} - 2h_{i-2}) + 3h_{i-1}^2}{(h_i + h_{i+1})(h_{i-1} + 2h_i + h_{i+1})\sigma_i}$$

$$+ 8\frac{h_{i-2}^2 + 4h_{i-1}h_{i-2} + h_i h_{i-2} + h_{i+2}(h_{i+2} - 2h_{i-1} - h_{i-2} + h_i)}{(h_i + h_{i+1})(h_{i-1} + 2h_i + h_{i+1})\sigma_i},$$

$$\alpha_i^{(0)} = -(\alpha_i^{(-1)} + \alpha_i^{(+1)}),$$

$$\alpha_i^{(+2)} = -\alpha_i^{(-2)},$$

$$\sigma_i = h_{i-2}^2 + h_{i+2}^2 + 2(h_{i-1}^2 + h_{i+1}^2) + 3(h_{i-1}h_{i-2} + h_{i+1}h_{i+2})$$

$$+ h_i(h_{i+1} + h_{i-1} + h_{i+2} + h_{i-2}) - h_{i-2}(h_{i+1} + h_{i+2}) - h_{i-1}(h_{i+1} + h_{i+2}),$$

The derivative approximation (5.2) reduces to the common three-point central difference whenever the grid is uniform around C_i.

For the discretization of the advection, we use the central upwind flux, see [28]. The discrete advection operator in the conservative formulation reads

$$\mathcal{A}_i(\mathbf{w}_h(t)) = -\frac{1}{h_i}\left(\mathcal{H}_{i+1/2}(\mathbf{w}_h(t)) - \mathcal{H}_{i-1/2}(\mathbf{w}_h(t)) \quad 0 \quad 0 \quad 0 \quad 0\right)^T. \quad (5.3)$$

The numerical fluxes $\mathcal{H}_{i+1/2}$, cf. (5.11), serve as approximations of the taxis fluxes between the cells C_i and C_{i+1}. They are given by products of the approximated characteristic velocities $\mathcal{P}_{i+1/2}$ with the reconstructions of the cancer cell densities on the cell interfaces. For $\mathcal{P}_{i+1/2}$ in particular, we compute:

$$\mathcal{P}_{i+1/2}(\mathbf{w}_h(t)) = \chi_u L_{i+1/2}(u_h(t)) + \chi_v L_{i+1/2}(v_h(t)) + \chi_p L_{i+1/2}(p_h(t)), \quad (5.4)$$

where $L_{i+1/2}$ represents central difference approximations of the first derivative. Since, 2nd order approximations cannot be obtained by a three point stencil on non-uniform grids, we employ a four point finite difference approximation centered around the interface, i.e.

$$L_{i+1/2}(u_h) = \beta_{i+1/2}^{(-1.5)}u_{i-1} + \beta_{i+1/2}^{(-0.5)}u_i + \beta_{i+1/2}^{(+0.5)}u_{i+1} + \beta_{i+1/2}^{(+1.5)}u_{i+2},$$

where the coefficients are chosen such that we get a third order accurate approximation of the first derivative,

$$
\beta_{i+1/2}^{(-1.5)} = \frac{h_{i+1}(6h_i - 4h_{i+1} - 2h_{i+2}) + 2h_i h_{i+2}}{(h_i + h_{i-1})(h_{i-1} + 2h_i + h_{i+1})(h_{i-1} + 2h_i + 2h_{i+1} + h_{i+2})},
$$

$$
\beta_{i+1/2}^{(-0.5)} = -\frac{h_{i+1}(12h_i + 6h_{i-1} - 2h_{i+2} - 4h_{i+1}) + h_{i+2}(2h_{i-1} + 4h_i)}{(h_{i-1} + h_i)(h_i + h_{i+1})(h_i + 2h_{i+1} + h_{i+2})},
$$

$$
\beta_{i+1/2}^{(+0.5)} = \frac{h_i(12h_{i+1} + 6h_{i+2} - 2h_{i-1} - 4h_i) + h_{i-1}(2h_{i+2} + 4h_{i+1})}{(h_{i+1} + h_{i+2})(h_i + h_{i+1})(h_{i-1} + 2h_i + h_{i+1})},
$$

$$
\beta_{i+1/2}^{(+1.5)} = -\frac{h_i(6h_{i+1} - 4h_i - 2h_{i-1}) + 2h_{i+1}h_{i-1}}{(h_{i+1} + h_{i+2})(h_i + 2h_{i+1} + h_{i+2})(h_{i-1} + 2h_i + 2h_{i+1} + h_{i+2})}.
$$

In order to approximate the gradient of c, we apply the *Monotonized Central* (MC) limiter [51] which reads on a uniform grid as:

$$
s_i(c_h) = \text{minmod}\left(2\frac{c_i - c_{i-1}}{h}, \ \frac{c_{i+1} - c_{i-1}}{2h}, \ 2\frac{c_{i+1} - c_i}{h}\right). \tag{5.5}
$$

where the minmod operator is given by

$$
\text{minmod}(v_1, \ldots, v_n) = \begin{cases} \max\{v_1, \ldots, v_n\}, & \text{if } v_k < 0, \ k = 1, \ldots, n, \\ \min\{v_1, \ldots, v_n\}, & \text{if } v_k > 0, \ k = 1, \ldots, n, \\ 0, & \text{otherwise.} \end{cases} \tag{5.6}
$$

For the case of non-uniform one dimensional grids, we define the *Generalized MC* (GMC) limiter as follows:

$$
s_i(c_h) = \text{minmod}\left(2\theta_i\frac{c_i - c_{i-1}}{\kappa_{i-1}}, \ \frac{-2\kappa_i c_{i-1}}{\kappa_{i-1}(\kappa_{i-1} + \kappa_i)} + \frac{2(\kappa_i^2 - \kappa_{i-1}^2)c_i}{\kappa_{i-1}\kappa_i(\kappa_{i-1} + \kappa_i)} + \frac{2\kappa_{i-1}c_{i+1}}{\kappa_i(\kappa_{i-1} + \kappa_i)}, \ 2\theta_i\frac{c_{i+1} - c_i}{\kappa_i}\right), \tag{5.7}
$$

where $\kappa_i = h_i + h_{i+1}$, and

$$
\theta_i = 1 + \frac{\min\{h_{i-1}, h_{i+1}\}}{h_i}. \tag{5.8}
$$

Remark 5.1. The middle term in (5.7) is a second order approximation of the first derivative of c at the center x_i of the cell C_i.

Whenever the grid is uniform, (5.8) yields $\theta_i = 2$ and (5.7) reduces to the usual uniform grid MC limiter (5.5). The reason for the local dependence of θ_i in (5.8) is that the usual MC limiter choice, i.e. $\theta_i = 2$ for every i in (5.7), can hamper the positivity of the solution over non-uniform grids. We hence set forth the following proposition, where we prove the maximum principle and *Total Variation Diminishing* (TVD) property of the proposed GMC limiter (5.7), (5.8).

The discretization of advection makes use of the linear reconstructions

$$
c_{i+1/2}^+ = c_i + \frac{h_i}{2}s_i(c_h), \quad c_{i+1/2}^- = c_{i+1} - \frac{h_{i+1}}{2}s_{i+1}(c_h). \tag{5.9}
$$

Proposition 5.1. α) *The interface reconstructions $c_{i+1/2}^\pm$ satisfy the maximum priciple, i.e. $c_i \leq c_{i+1/2}^+, c_{i+1/2}^- \leq c_{i+1}$ for increasing data $c_i \leq c_{i+1}$ and $c_i \geq c_{i+1/2}^+, c_{i+1/2}^- \geq c_{i+1}$ for decreasing data $c_i \geq c_{i+1}$.*

β) *We consider for a constant $\alpha > 0$ the linear transport equation*

$$
\partial_t c + \alpha \partial_x c = 0,
$$

being resolved by the upwind scheme

$$
c_i^{n+1} = c_i^n - \frac{\tau\alpha}{h_i}(c_{i+1/2}^+ - c_{i-1/2}^+).
$$

11

If the CFL condition

$$\min_{1 \leq i \leq N} \frac{\alpha\tau}{h_i} \leq \frac{1}{2}$$

holds, the numerical solution satisfies the TVD property:

$$\sum_{i=1}^{N-1} |c_{i+1}^{n+1} - c_i^{n+1}| \leq \sum_{i=1}^{N-1} |c_{i+1}^n - c_i^n|.$$

Proof. α) Equation (5.7) yields

$$\begin{cases} 0 \leq s_i \leq \mathrm{minmod}\left(2k_i^+ \dfrac{c_{i+1} - c_i}{h_i}, \ 2k_i^- \dfrac{c_i - c_{i-1}}{h_i}\right), & \text{if either } c_i \leq c_{i+1} \text{ or } c_{i-1} \leq c_i, \\[3mm] 0 \geq s_i \geq \mathrm{minmod}\left(2k_i^+ \dfrac{c_{i+1} - c_i}{h_i}, \ 2k_i^- \dfrac{c_i - c_{i-1}}{h_i}\right), & \text{if either } c_i \geq c_{i+1} \text{ or } c_{i-1} \geq c_i, \end{cases} \tag{5.10}$$

where

$$k_i^+ = \frac{h_i + \min\{h_{i-1}, h_{i+1}\}}{h_i + h_{i+1}}, \quad k_i^- = \frac{h_i + \min\{h_{i-1}, h_{i+1}\}}{h_{i-1} + h_i}, \quad 0 \leq k_i^+, k_i^- \leq 1.$$

Thus for $c_i < c_{i+1}$, where $s_i, s_{i+1} \geq 0$, we get

$$c_i \leq c_{i+1/2}^+ \leq c_i + k_i^+(c_{i+1} - c_i) \leq c_{i+1},$$
$$c_{i+1} \geq c_{i+1/2}^- \geq c_{i+1} - k_{i+1}^-(c_{i+1} - c_i) \geq c_i.$$

And similarly for $c_i > c_{i+1}$, where $s_i, s_{i+1} \leq 0$,

$$c_i \geq c_{i+1/2}^+ \geq c_i + k_i^+(c_{i+1} - c_i) \geq c_{i+1},$$
$$c_{i+1} \leq c_{i+1/2}^- \leq c_{i+1} - k_{i+1}^-(c_{i+1} - c_i) \leq c_i.$$

β) We follow [6] and first show that local maxima decrease. Secondly we prove that a monotonically increasing solution remains monotone. It can be shown analogously that monotonically decreasing solutions remains monotonically decreasing and that local minima increase.

We first consider the local maximum case $c_{i-1}^n < c_i^n$, $c_i > c_{i+1}^n$. In this case the slope is limited by (5.7), $s_i = 0$ and $s_{i-1} \geq 0$. The updated cell average can be estimated using (5.10):

$$c_i^{n+1} = c_i^n - \lambda_i \left(c_i^n - c_{i-1}^n - \frac{s_{i-1}^n h_i}{2}\right) \leq c_i^n - \lambda_i \left(c_i^n - c_{i-1}^n - k_{i-1}^+(c_i^n - c_{i-1}^n)\right) \leq c_i^n,$$

where $\lambda_i = \frac{\tau\alpha}{h_i}$.

Next, we consider monotonically increasing cell averages $c_{i-1} \leq c_i \leq c_{i+1}$. Using the first property of the proposition, we get $c_i^{n+1} \leq c_i^n - \lambda_i(c_i^n - c_i^n) = c_i^n$. We derive also a lower bound,

$$c_i^{n+1} = c_i^n - \lambda_i \left(c_i^n + \frac{h_i s_i}{2} - \left(c_{i-1}^n + \frac{h_{i-1} s_{i-1}}{2}\right)\right) \geq c_i^n - \lambda_i \left(c_i^n + k_i^+ \left(c_i^n - c_{i-1}^n\right)\right) + \lambda_i c_{i-1}^n$$
$$\geq (1 - 2\lambda_i)c_i^n + 2\lambda_i c_{i-1}^n \geq c_{i-1}^n$$

where the restriction $\lambda_i \leq \frac{1}{2}$ has been used. We conclude that $c_{i-1}^{n+1} \leq c_{i-1}^n \leq c_i^{n+1} \leq c_i^n \leq c_{i+1}^{n+1} \leq c_{i+1}^n$. Hence the solution remains monotone.

$\square$

The numerical fluxes which we use are based on the upwind approach and are given as follows

$$\mathcal{H}_{i+1/2}(\mathbf{w}_h) = \begin{cases} \mathcal{P}_{i+1/2}(\mathbf{w}_h) c_{i+1/2}^+, & \text{if } \mathcal{P}_{i+1/2}(\mathbf{w}_h) \geq 0, \\ \mathcal{P}_{i+1/2}(\mathbf{w}_h) c_{i+1/2}^-, & \text{if } \mathcal{P}_{i+1/2}(\mathbf{w}_h) < 0. \end{cases} \tag{5.11}$$

In the two-dimensional case we consider uniform, quadrilateral meshes. Therefore we can employ the above numerical fluxes for advection using dimensional splitting. We further discretize the Laplace operator with common five point finite differences on these meshes.

After space discretization, we end up with the following system of ordinary differential equations

$$\partial_t \mathbf{w}_h = \mathcal{A}(\mathbf{w}_h) + \mathcal{R}(\mathbf{w}_h) + \mathcal{D}(\mathbf{w}_h). \tag{5.12}$$

Time discretization. The numerical approximations of the solution of (5.12) at discrete points in time t^n will be denoted as $\mathbf{w}_h^n$.

The discretization of the taxis-terms dictates a limit on the time step $\tau_n = t^{n+1} - t^n$ according to the CFL condition

$$\max_{i,\pm} \ \tau_n \frac{\mathcal{P}_{i\pm1/2}(\mathbf{w}_h^n)}{h_i} = \text{CFL} \leq 1. \tag{5.13}$$

We have compared several numerical methods to approximate (5.12). They are shortly described in the following part.

EXPLICIT: The first order forward Euler time integration

$$\mathbf{w}_h^{n+1} = \mathbf{w}_h^n + \tau_n \left(\mathcal{A}(\mathbf{w}_h^n) + \mathcal{R}(\mathbf{w}_h^n) + \mathcal{D}(\mathbf{w}_h^n) \right).$$

This is the only explicit method, we apply. It requires small time steps for stability reasons due to the explicit discretization of diffusion. Indeed, $\tau_n = \mathcal{O}(\max_i h_i^2)$.

CND: A Crank-Nicolson type method with

$$\mathbf{w}_h^{n+1} - \frac{\tau_n}{2} \mathcal{D}(\mathbf{w}_h^{n+1}) = \mathbf{w}_h^n + \tau_n \left(\frac{1}{2} \mathcal{D}(\mathbf{w}_h^n) + \mathcal{R}(\mathbf{w}_h^n) + \mathcal{A}(\mathbf{w}_h^n) \right).$$

Since we approximate the diffusion term implicitly, and the reaction term is not stiff we can choose the time steps according to the CFL condition (5.13) alone.

ROSENBROCK: A general s-stage linearly implicit or Rosenbrock method takes the form:

$$\begin{cases} \mathbf{w}_h^{n+1} = \mathbf{w}_h^n + \tau_n \sum_{j=1}^{s} b_j k_j, \\ (Id - a_{j,j}\tau_n \ J)k_j = g(\mathbf{w}_h^n + \tau_n \sum_{\nu=1}^{j-1}(a_{j,\nu} + \gamma_{j,\nu})k_\nu) - \tau_n J \sum_{\nu=1}^{j-1} \gamma_{j,\nu} k_\nu, \quad j = 1, \ldots, s. \end{cases} \tag{5.14}$$

for given lower triangular matrices $A = (a_{i,j})_{i,j=1}^s$, $\Gamma = (\gamma_{i,j})_{i,j=1}^s$, a vector b and

$$g(\mathbf{w}_h) = \mathcal{A}(\mathbf{w}_h^n) + \mathcal{R}(\mathbf{w}_h^n) + \mathcal{D}(\mathbf{w}_h^n).$$

If A, b satisfy specific algebraic conditions, high order of consistency can be reached with these methods. Stability properties can be achieved by selecting reasonable values for the parameter matrix Γ and a suitable approximation J of $\frac{\partial}{\partial \mathbf{w}_h}(g(\mathbf{w}_h))$ [14]. We choose $J = \frac{d}{d\mathbf{w}_h}(\mathcal{R}(\mathbf{w}_h^n) + \mathcal{D}(\mathbf{w}_h^n))$ since we assume the taxis discretization to be stable in explicit methods.

ROS2: An L-stable, second order consistent two stage Rosenbrock method ($s = 2$), which has been used for applications in reaction-diffusion-taxis systems in [16]. It is given by the coefficients

$$A = \begin{pmatrix} 1 - \frac{\sqrt{2}}{2} & 0 \\ \sqrt{2} - 1 & 1 - \frac{\sqrt{2}}{2} \end{pmatrix}, \ \Gamma = \begin{pmatrix} 0 & 0 \\ 2 - \sqrt{2} & 0 \end{pmatrix}, \ b = \begin{pmatrix} \frac{1}{2} & \frac{1}{2} \end{pmatrix}^T. \tag{5.15}$$

13

$$
\begin{array}{c|ccc}
0 & 0 & & \\
\frac{1}{2} & \frac{1}{4} & \frac{1}{4} & \\
1 & \frac{1}{3} & \frac{1}{3} & \frac{1}{3} \\
\hline
1 & \frac{1}{3} & \frac{1}{3} & \frac{1}{3}
\end{array}
$$

Table 5.1: *Butcher tableau for the simplified TR-BDF2 method.*

ROS3: An L-stable [21] third order Rosenbrock method ($s = 3$) with coefficients

$$
A = \begin{pmatrix} a & 0 & 0 \\ 0.5 & a & 0 \\ 0.5 & 0.5 & a \end{pmatrix}, \quad \gamma_{2,1} = -(3a + \gamma_{3,1} + \gamma_{3_2}),
$$

$$
a = 1 - \frac{1}{2}\sqrt{2}\cos(\theta) + \frac{1}{2}\sqrt{6}\sin(\theta), \quad \gamma_{3,2} = \frac{1}{2} - 3a,
$$

$$
b = \begin{pmatrix} \frac{1}{3} & \frac{1}{3} & \frac{1}{3} \end{pmatrix}^T, \quad \gamma_{3,1} = -\frac{1}{1 + 2\gamma_{3,2}}\left(6a^3 - 12a^2 + 6(1 + \gamma_{3,2})a + 2\gamma_{3,2}^2 - \frac{1}{2}\right),
$$

$$
\theta = \frac{1}{3}\arctan\left(\frac{\sqrt{2}}{4}\right).
$$

ROS3-ATC: The ROS3 method with Adaptive Time step Control (ATC).

STRANG: A second order splitting approach. Let $\Xi_{\mathcal{F}}(\tau)y$ be a numerically approximated solution of the initial value problem

$$
\partial_t \mathbf{w}_h = \mathcal{F}(\mathbf{w}_h), \quad \mathbf{w}_h(0) = y,
$$

at $t = \tau$, for any operator introduced before, $\mathcal{F} \in \{\mathcal{D}, \ \mathcal{R}, \ \mathcal{A}\}$. The Strang-splitting method yields

$$
\mathbf{w}_h^{n+1} = \Xi_{\mathcal{T}}\left(\frac{\tau_n}{2}\right)\Xi_{\mathcal{D}}\left(\frac{\tau_n}{2}\right)\Xi_{\mathcal{R}}(\tau_n)\Xi_{\mathcal{D}}\left(\frac{\tau_n}{2}\right)\Xi_{\mathcal{T}}\left(\frac{\tau_n}{2}\right)\mathbf{w}_h^n. \tag{5.16}
$$

This method is known to be second order accurate in time, if the methods used to compute $\Xi_{\mathcal{F}}(\tau_n)$, are at least second order. We choose the fourth order Runge-Kutta method [18] for the reaction- and taxis-step and the TR-BDF2 method (modified trapezoidal rule with the second order backward differential formula) for the diffusion-terms. The TR-BDF2 can be written as an imlicit Runge-Kutta method, coefficients can be found in Table 5.1.

STRANG-IR: A variant of the *STRANG* method: it employs the linearly implicit second order method *ROS2* for the reaction term instead of the explicit Runge-Kutta method.

IMEX3: A third order implicit-explicit method following [37]. We consider a splitting of the ordinary differential equation into an implicit part $\mathcal{I}$ and an explicit part $\mathcal{E}$,

$$
g(\mathbf{w}_h) = \mathcal{A}(\mathbf{w}_h^n) + \mathcal{R}(\mathbf{w}_h^n) + \mathcal{D}(\mathbf{w}_h^n) = \mathcal{I}(\mathbf{w}_h) + \mathcal{E}(\mathbf{w}_h),
$$

where $\mathcal{I} = \mathcal{D}$ and $\mathcal{E} = \mathcal{A} + R$, and apply an explicit Runge-Kutta method for the explicit part and a coupled diagonally implicit Runge-Kutta-method to the implicit part resulting in an Implicit-Explicit (IMEX) scheme. A general s-stage scheme reads

$$
\begin{cases}
\mathbf{W}_i^* = \mathbf{w}_h^n + \tau_n \sum_{j=1}^{i-2} \bar{a}_{i,j}\mathbf{E}_j + \tau_n \ \bar{a}_{i,i-1}\mathbf{E}_{i-1}, & i = 1, \dots, s, \\[2ex]
\mathbf{W}_i = \mathbf{W}_i^* + \tau_n \sum_{j=1}^{i-1} a_{i,j}\mathbf{I}_j + \tau_n a_{i,i}\mathbf{I}_i, & i = 1, \dots, s, \\[2ex]
\mathbf{w}_h^{n+1} = \mathbf{w}_h^n + \tau_n \ \sum_{i=1}^{s} \bar{b}_i\mathbf{E}_i + \tau_n \ \sum_{i=1}^{s} b_i\mathbf{I}_i,
\end{cases} \tag{5.17}
$$

$$
\begin{array}{c|cccc}
0 & & & & \\
\dfrac{1767732205903}{2027836641118} & \dfrac{1767732205903}{2027836641118} & & & \\
\dfrac{3}{5} & \dfrac{5535828885825}{10492691773637} & \dfrac{788022342437}{10882634858940} & & \\
1 & \dfrac{6485989280629}{16251701735622} & -\dfrac{4246266847089}{9704473918619} & \dfrac{10755448449292}{10357097424841} & \\
\hline
 & \dfrac{1471266399579}{7840856788654} & -\dfrac{4482444167858}{7529755066697} & \dfrac{11266239266428}{11593286722821} & \dfrac{1767732205903}{4055673282236}
\end{array}
$$

$$
\begin{array}{c|cccc}
0 & 0 & & & \\
\dfrac{1767732205903}{2027836641118} & \dfrac{1767732205903}{4055673282236} & \dfrac{1767732205903}{4055673282236} & & \\
\dfrac{3}{5} & \dfrac{2746238789719}{10658868560708} & -\dfrac{640167445237}{6845629431997} & \dfrac{1767732205903}{4055673282236} & \\
1 & \dfrac{1471266399579}{7840856788654} & -\dfrac{4482444167858}{7529755066697} & \dfrac{11266239266428}{11593286722821} & \dfrac{1767732205903}{4055673282236} \\
\hline
 & \dfrac{1471266399579}{7840856788654} & -\dfrac{4482444167858}{7529755066697} & \dfrac{11266239266428}{11593286722821} & \dfrac{1767732205903}{4055673282236}
\end{array}
$$

Table 5.2: *Tableau for the explicit (first tableau) and the implicit part (second tableau) of the third order IMEX-Runge-Kutta scheme (IMEX3).*

where $\mathbf{E}_i = \mathcal{E}(\mathbf{W}_i)$, $\mathbf{I}_i = \mathcal{I}(\mathbf{W}_i)$, $i = 1,\ldots,s$. The explicit scheme is given by $\bar{b}$, $\bar{A}$, and the diagonally implicit scheme by b, A.

We consider a third order four-stage scheme ($s = 4$ in (5.17)) constructed in such a way that it fulfills several stability conditions, e.g. L-stability [23]. The corresponding coefficients can be found in Table 5.2.

IMEX3-ATC: Third order IMEX method with adaptive time step control. This method is applied in two further variants: *IMEX3-ATC-UPWIND1* uses first order upwind fluxes ($s_i(c_h) = 0$ in (5.11)), *IMEX3-ATC-IR* treats reaction terms implicitly and uses $\mathcal{I} = \mathcal{D} + \mathcal{R}$.

Adaptivity in time. Adaptive time step control is done conventionally by employing an additional lower order scheme in order to calculate a local error estimate

$$\varepsilon_n = \|\mathbf{w}_h^{n+1} - \mathbf{w}_h^{n+1,\,\text{low}}\|_1. \tag{5.18}$$

The approximation w_h^{n+1} is then rejected if

$$\varepsilon_n \geq \varepsilon_n^{\text{tol}} = \max\{10^{-6},\ 10^{-6}\,\|w_h^n\|_1\}, \tag{5.19}$$

otherwise it is accepted. In both cases, the time step τ_n is updated as

$$\tau^{\text{new}} = \min\left\{ 0.9\ \sqrt[p+1]{\frac{\varepsilon_n^{\text{tol}}}{\varepsilon_n}}\ \tau^{\text{old}}, \min_{i,\pm} \frac{h_i\,\text{CFL}}{\mathcal{P}_{i\pm 1/2}} \right\}, \tag{5.20}$$

where the integer p refers to the order of accuracy of the method which is used to compute the comperative solution $\mathbf{w}_h^{n,\,\text{low}}$, and where h_i and $\mathcal{P}_{i\pm 1/2}$ are updated only after an accepted time step.

We consider adaptive time step control for the third order linearly implicit scheme and the third order IMEX-Runge-Kutta scheme. Both of them are third order methods and feature an embedded method of second order ($p = 2$). Hence, lower order approximations ($\mathbf{w}_h^{n+1,\,\text{low}}$) can be obtained without much additional computational costs. Weights β which replace the regular weights b in the lower order embedded schemes are given by

$$\bar{\beta} = \beta = \left(\tfrac{2756255671327}{12835298489170} \quad -\tfrac{10771552573575}{22201958757719} \quad \tfrac{9247589265047}{10645013368117} \quad \tfrac{2193209047091}{5459859503100} \right)^T,$$

for the IMEX3 scheme, and by

$$\beta = \left(\tfrac{1}{2} \quad \tfrac{1}{2} \quad 0 \right)^T,$$

15

for the ROS3 scheme.

We have examined in this paragraph, numerous time integration methods with different properties in order to identify suitable choices for the numerical simulation of systems like (3.6), (4.2), and (4.4) when combined with the space discretization, introduced previously. We include methods of first order (EXPLICIT, CND), second order (ROS2, STRANG and STRANG-IR) and of third order (ROS3, IMEX3 and variations). Concerning the diffusion term, the methods ROS3, STRANG, STRANG-IR and IMEX3 are L-stable, which is favourable in diffusion problems, cf. [21], while ROS2 and CND are A-stable only. Except for EXPLICIT and the ATC variations, all methods use only the CFL condition (5.13) to determine the time steps, i.e. we expect them to necessitate similar number of time steps. Since the ATC technique is an additional condition on top of the CFL, we expect the ATC methods to use more time steps in general and thus to be more expensive but more accurate. We also expect EXPLICIT to be expensive since it necessitates time steps of order $(\frac{1}{N})^2$. Several methods treat the reaction terms implicitly (ROS2, ROS3, STRANG-IR, IMEX3-ATC-IR) which might cause additional computational burden in the case of (3.6) since less sparse matrices are used in the computations. An exceptional case, for demonstrating the advantages of our second order advection discretization, is the IMEX3-ATC-UPWIND1 method which combines third order time integration with first order fluxes in space.

Adaptivity in space. We constrain, in this work, the adaptation of the mesh to the 1-dimensional case, and postpone the treatment of the 2-dimensional case for a subsequent paper.

We consider a (in general) non-uniform grid where the computational cells (their total number, position, and size) depend also on the time t^n. We use in particular the following notation regarding the discretization of the domain:

$$\Omega = \bigcup_{i=1}^{N_n} C_i^n, \quad |C_i^n| = h_i^n.$$

where N_n is the total number of computational cells at the time instance t^n.

For the handling of the grid, we employ an h-refinement Adaptive Mesh Refinement (AMR) method with cell bisection. Due to the cell bisection, the h-refinement leads to the creation of a dyadic tree, to each level of which a different *level of refinement* number (to be clarified subsequently) is assigned. We set $\mathcal{L}_i^n$ to represent the refinement level of the cell C_i^n (see also [27, 41]). The main components of h-refinement, as we employ it, are the following:

Grid initialization: We set an initial computational grid comprised of N_0 equivalent computational cells C_i^0. We assign the 0th level of refinement in each cell, i.e. $\mathcal{L}_i^0 = 0$ for every $i = 1, \ldots, N_0$. The initial conditions are evaluated over this mesh.

Monitor function computation: We compute, on each cell, the value of a *monitor function* $M_i(\cdot)$ that depends on the numerical solution $\mathbf{w}_h^n$ and drives the subsequent refinement/coarsening process.

The monitor functions we employ in this work are either based on geometric properties of the numerical solutions, like the discrete gradient of c,

$$M_i(\mathbf{w}_h) = \max \left\{ \left| 2\frac{c_{i+1}^n - c_i^n}{h_{i+1}^n + h_i^n} \right|, \left| 2\frac{c_i^n - c_{i-1}^n}{h_i^n + h_{i-1}^n} \right| \right\}, \tag{5.21}$$

or, its discrete local variation

$$M_i(\mathbf{w}_h) = \max \left\{ \left| c_{i+1}^n - c_i^n \right|, \left| c_i^n - c_{i-1}^n \right| \right\}, \tag{5.22}$$

or even based on properties of the model like (the hierarchical error estimator of) the characteristic velocities (5.4):

$$M_i(\mathbf{w}_h) = \max \left\{ \left| \mathcal{P}_{i-1/2}^n - \mathcal{P}_{i+1/2}^{n,\text{low}} \right|, \left| \mathcal{P}_{i+1/2}^n - \mathcal{P}_{i+1/2}^{n,\text{low}} \right| \right\}, \tag{5.23}$$

where the lower order approximations $\mathcal{P}_{i+1/2}^{n,\text{low}}$ are computed using two point approximations of the first derivative, and the higher order $\mathcal{P}_{i+1/2}^n$ by using (5.4).

We have seen that geometric estimators like (5.21) and (5.22) are more robust and problem independent than model-driven estimators (5.23), see also [5, 27, 41, 43].

Refinement/Coarsening: We set predefined thresholds $C_{coa} < C_{ref}$, which when violated by the monitor function (above or below) the corresponding cells are marked for refinement/coarsening. In particular:

- If $M_i(\mathbf{w}_h^n) > C_{ref}$ the cell C_i^n is marked for refinement. A *mother cell* C_i^n, of refinement level $\mathcal{L}_i^n = k$, when refined (bisected), yields two isodynamous *daughter cells* of level of refinement $k + 1$. Approximate values of the monitor function (using the mother cell) are computed on the daughter cells, and the refinement process is repeated (at most) n_{ref} times. We prescribe a maximal level of refinement $\mathcal{L}_{max}$ beyond which no further refinement is allowed.

- If $M_i(\mathbf{w}_h^n) < C_{coa}$ the cell C_i^n is marked for coarsening. A cell is coarsened only if its *sibling cell* (the cell with which it shares the same mother cell) has also been marked for coarsening. Approximate values of the monitor function on the (coarse) mother cell are computed by the daughter cells, and the coarsening process is repeated (at most) n_{coar} times. Cells that have just been refined are prevented from being coarsened. Cells of refinement level $\mathcal{L}_i^n = 0$ can not be coarsened; the local resolution of grid cannot become coarser than the initial grid.

Grid smoothness: During our numerical investigations, we have noticed that *smoothly varying grids* perform better in terms of error approximation (in this type of problems). Smoothly varying grids are the non-uniform grids, where neighbour cells differ by at most 1 level of refinement, i.e.

$$|\mathcal{L}_i^n - \mathcal{L}_{i+1}^n| \leq 1, \quad i = 1, \ldots, N_n - 1. \tag{5.24}$$

We impose this smoothness condition with an iterative process by enforcing refinement of the neighbour cells, or by preventing further coarsening of the current cell. We refer to the Section 6.4 for more details.

Solution update: The numerical solutions are updated on the new grid. If a cell of the new grid is a result of coarsening (i.e a mother cell), the corresponding new numerical value is obtained by (mass conservative) averaging of the numerical solution over its daughter cells. If a new cell is the result of refinement (i.e. a daughter cell), the corresponding new numerical value is obtained by a mass conservative projection of the piecewise polynomial solution from the mother cell to the daughter cell. In more detail, we construct a second order polynomial , that interpolates the masses of the mother cell and its two neighbour cells, from which we project the masses to the new daughter cells. No change is needed if a cell has not been altered by the refinement process. The solution update step takes place after each one of the n_{ref}, n_{coar} refinement/coarsening processes; the monitor function is computed on the new mesh before every subsequent refinement/coarsening.

Time evolution: The numerical solution evolves in time with time steps that are uniform in space, thus the same τ_n is used for all cells. These time steps are computed by the CFL and by other stability conditions needed by the chosen time integration method. The numerical methods used are adjusted to non-uniform grids.

As most AMR methods, h-refinement alternates between the manipulation of the grid and the time evolution of the numerical solution, so, after a successful completion of the *Time evolution* step, the process is repeated with the *Monitor function computation* step. Before the first *Time evolution* takes place, the solution is (at most) n_{ini} times initially refined by proceeding according to the *Refinement/Coarsening* step while making use of the initial data in the *Solution update*.

6   Numerical study

In this section, we present results of numerical simulations[*], compare the performance of the methods introduced previously, and demonstrate the capabilities of the h-refinement.

---

[*]All numerical experiments were conducted using MATLAB.

6.1 Experiment I

Our aim with this experiment is to compare the time integration methods described in Sect. 5. To that end, we consider the system (3.6) on the one-dimensional interval $\Omega = (0, 10)$ together with homogeneous Neumann boundary conditions. The parameters are chosen according to the parameter set $\mathcal{P}$ (3.9). The following initial conditions are used:

$$
\begin{cases}
c_0(x) = \exp\left(\frac{-x^2}{\varepsilon}\right), \\
v_0(x) = 1 - \frac{1}{2}\exp\left(\frac{-x^2}{\varepsilon}\right), \\
u_0(x) = \frac{1}{2}\exp\left(\frac{-x^2}{\varepsilon}\right), \\
p_0(x) = \frac{1}{20}\exp\left(\frac{-x^2}{\varepsilon}\right), \\
m_0(x) = 0,
\end{cases}
\qquad x \in (0, 10), \tag{6.1}
$$

where $\varepsilon = 5 \times 10^{-3}$. The initial conditions can be interpreted as an accumulation of cancer cells c, which start their invasion from the left boundary of the domain. The ECM v is mostly intact, except for the location of the cancer cell accumulation. Activation of the plasmin m has not taken place up to $t = 0$, but the urokinase u and a smaller amount of PAI-1, p, is already on the spot everywhere, where cancer cells are located.

Figure 6.1 shows the computed time evolution of all the components of the system during the period $t \in [0, 500]$. A cluster of cancer cells travels to the right degenerating at the same time the ECM. In areas, where vitronectin is already degenerated to a small level, new clusters, which take the form of peaks in the cancer cell densities, emerge. This can already be seen at $t = 25$. The number of these peaks as well as their heights in c vary in time. Clusters not only emerge, but they also move and merge. By $t = 75$ almost half of the domain is invaded by the cancer cells and even when the entire domain is invaded, the cancer cell density exhibits a dynamically heterogeneous spatio-temporal behavior, which can be seen by comparison at $t = 300$ and $t = 500$. The enzymes of the uPA-system, which regulate the process of invasion, do not develop isolated clusters and take densities between 0 and 1 throughout the period $t \in [0, 500]$. The inhibitor PAI-1 density stays smooth mostly, while uPA and plasmin develop spiky solutions, as they are more directly influenced by the cancer cells. For the computation, we have employed the numerical method described in Section 5, over a computational grid of 5000 cells along side with IMEX3 for the time integration.

In order to compare different time integration methods, we consider the shorter domain $(0, 5)$ and the final time $T = 60$. We will study how the methods, described in the previous section, perform in this case. For comparison reasons, we consider a fixed Courant number of CFL=0.49 for every method.

Since the exact solution is not known, we compute a reference solution $\mathbf{w}^{\mathrm{ref}}$ on a very fine grid with $30\,000$ uniform cells C_i^{ref}, $i = 1, \ldots, 30\,000$ using our space discretization (cf. Section 5). In order to further minimize the temporal error, the reference solution is computed using the high order method of Dormand and Prince [18] along side with ATC adjusted to preserve the positivity of the numerical solution[†] and a strict tolerance of 10^{-12}. We are only interested in a solution at time T and thus we drop the time index and denote by $\mathbf{w}_i^{\mathrm{ref}}$ the reference solution at $T = 60$ on the cell C_i^{ref}, the corresponding piecewise constant approximation by $\mathbf{w}^{\mathrm{ref}}$ and its first component, the cancer cell density, by c^{ref}. To compare the accuracy of the introduced methods in space, we compute the discrete L^1-errors of the cancer cell densities:

$$
E(N) := |c^{\mathrm{ref}} - c^N|_{L^1_{\mathrm{disc}}(\Omega)} = \sum_{i=1}^{N} \left|C_i^N\right| \, |c_i^N - c^{\mathrm{ref}}(x_i)|, \tag{6.2}
$$

[†]We accept a time step if both criteria $\varepsilon_n < \varepsilon_n^{\mathrm{tol}}$, and $\min_i \mathbf{w}_i^n \geq 0$ hold. In the case $\varepsilon_n < \varepsilon_n^{\mathrm{tol}}$, and $\min_i \mathbf{w}_i^n < 0$ we repeat the time integration step using $\tau^{\mathrm{new}} = 0.8\,\tau^{\mathrm{old}}$. In all other cases we proceed according to the standard ATC (cf. Section 5).
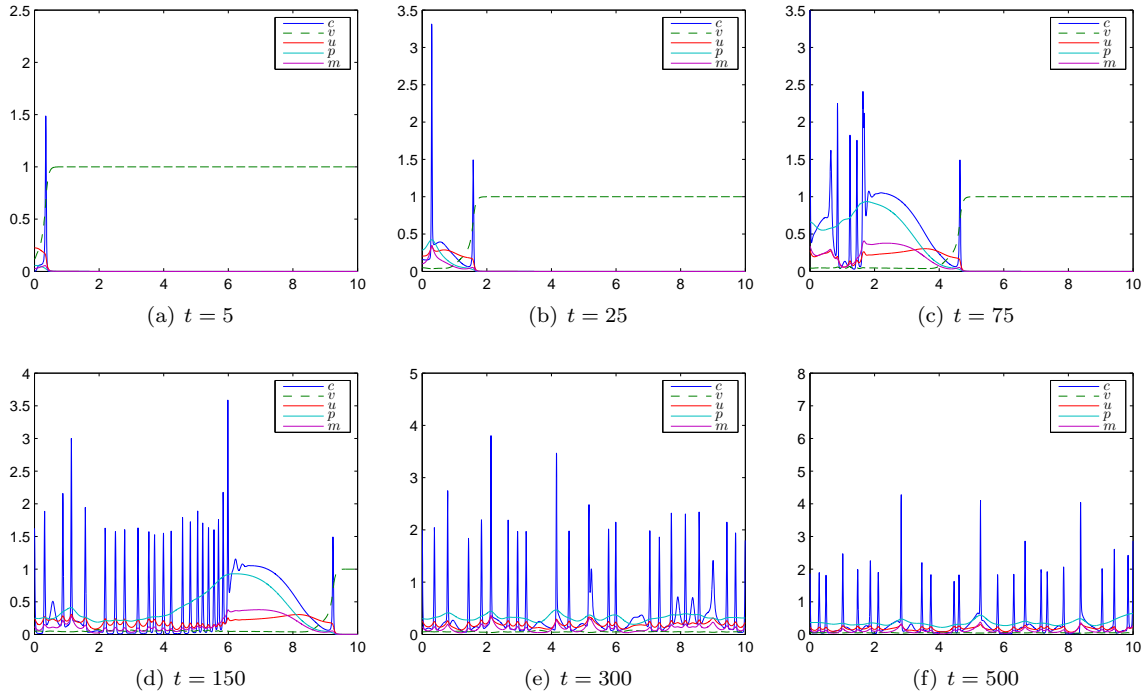
Figure 6.1: *(Exp. I) Overview of the dynamics of the system* (3.6) *(over space x) with parameter set* $\mathcal{P}$ *with* $D_c = 3.5 \ 10^{-4}$. *A uniform space discretization (cf. Section 5) with* $N = 5000$ *cells and IMEX3 time integration were employed.*

where w^N with its first component c^N is a numerical solution on N uniform cells $C_1^N, \ldots, C_N^N$ with cell centers $x_1, \ldots, x_N$.

The error of each method we are going to compare, consists of a spacial and a temporal component. Most methods we use determine their time steps according to the CFL condition (5.13) alone. In these "CFL-based" cases, the temporal part of the error is proportional to the cell size, i.e.

$$|c^{\text{ref}} - c^N|_{L^1_{\text{disc}}(\Omega)} \leq C_1 \tau^p + C_2 \left(\frac{1}{N}\right)^q \leq C \left(\frac{1}{N}\right)^{\min\{p,\, q\}}, \qquad (6.3)$$

where p and q denote the orders in time and space of the method used to compute c^N, and τ is the maximal time step used up to T. In the case of explicit diffusion, which is employed in the EXPLICIT method, time steps are further reduced for stability and the term $C_1 \tau^p$ in (6.3) can be estimated by $C_1 \left(\frac{1}{N}\right)^{2p}$ from above whereas the heuristic estimate $C_1 \tau^p \leq \tilde{C}_1 T \varepsilon^{tol}$ holds in the ATC case. We expect $E(N)$ to be of order two for all tested methods which make use of our second order space discretization, except for CND, which is only first order accurate in time. For the IMEX3-ATC-UPWIND1 method $E(N)$ should exhibit a first order convergence despite the high order time discretization, since it employs numerical fluxes of first order only.

To verify this convergence behaviour, we compute numerical solutions on N cells for each method for

$$N \in \{100,\ 200,\ 400,\ 800,\ 1000,\ 2000,\ 3000,\ 4000,\ 5000\}$$

and plot $E(N)$ against N in log-log scale in order to visualize the convergence of the method experimentally. We restrict our numerical experiments to $N = 5000$ due to the limitations of the comparison of numerical simulations with reference solutions computed over very fine grids; it has been seen experimentally that the number of grid cells of the numerical solutions should not exceed the 10% of the number of cells of the reference solution.

Figure 6.2 indicates that CND does not compute acceptable approximations, although a first order convergence can be observed. STRANG, IMEX3, ROS2, and ROS3 seem to converge second order in
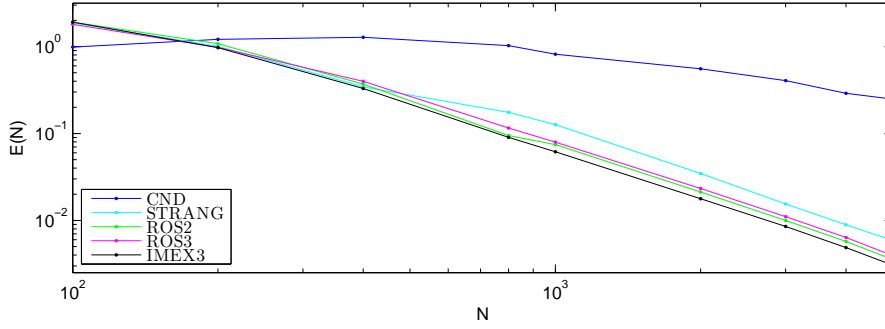
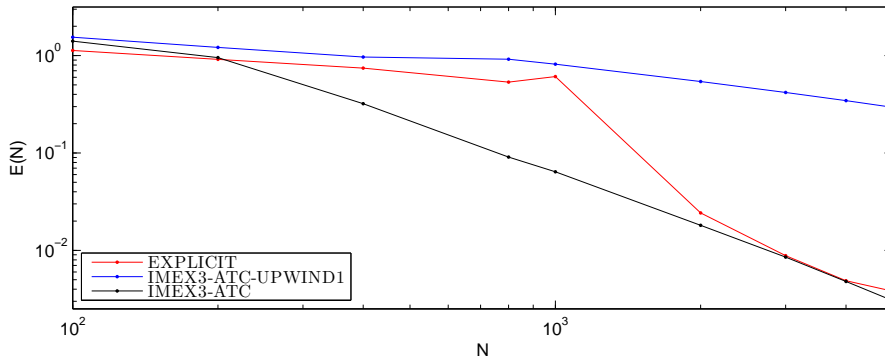Figure 6.2: *(Exp. I) Experimental convergence plot of "CFL-based" methods.*

Figure 6.3: *(Exp. I) Experimental convergence plot of non "CFL-based" methods.*

space. In particular, IMEX3 gives better results than STRANG. Surprisingly, the two stage Rosenbrock method gives a slightly better accuracy, than the three stage Rosenbrock method.

In Figure 6.3 a slow convergence of the IMEX3 method with first order upwind fluxes can be observed; it does not produce accurate approximations. The EXPLICIT method however performs better, especially for more than 2000 computational cells. Both are outperformed by IMEX3-ATC for which a second order convergence can be seen. Though, the additional computational costs for IMEX3-ATC prevails the slight advantage in accuracy for large N compared to IMEX3.

Table 6.1 gives an overview of the experimental orders of convergence (EOC), the absolute discrete L^1-error of a sample solution with 2000 cells, and the corresponding computational times. The EOCs are calculated by the discrete L^1-errors for $N_1 = 2000$ and $N_2 = 4000$ cells

$$EOC = \frac{\log(E(N_1)) - \log(E(N_2))}{\log(N_2) - \log(N_1)}. \tag{6.4}$$

The computed EOC numbers verify our previous expectations. The computational costs of IMEX3 are less than the those of ROS2 and ROS3, since in the latter the linearly implicit method handles reaction-terms implicitly and this makes them solve systems of linear equations with less sparse matrices. Similarly the variations of STRANG and IMEX3-ATC that employ implicit methods for the reaction terms (STRANG-IR and IMEX3-ATC-IR) are significantly more expensive albeit slightly more accurate. The time adaptive ATC methods (using an absolute and relative tolerance of 10^{-6}) do not offer considerable advantages over the "CFL-based" methods in terms of error and EOC while they are substantially more expensive. All methods we employed delivered non negative results at the final time T. However STRANG and STRANG-IR are the only methods we used for which the solution stays non negative for all time steps between 0 and T. Due to their accuracy and relatively low computational costs (see Table 6.1), we promote IMEX3, and STRANG since it also preserves positivity, as our favorite methods of choice.

20

	EOC	rel. CPU times	discrete L^1 error
CND	1.162	0.32	5.544×10^{-1}
IMEX3-ATC-UPWIND1	0.675	0.89	5.414×10^{-1}
STRANG	1.925	1	3.472×10^{-2}
STRANG-IR	1.927	3.26	3.422×10^{-2}
EXPLICIT	2.067	3.24	2.425×10^{-2}
ROS3	1.919	4.52	2.331×10^{-2}
ROS2	1.942	3.03	2.125×10^{-2}
IMEX3-ATC	2.009	3.68	1.810×10^{-2}
IMEX3-ATC-IR	1.930	348.01	1.794×10^{-2}
ROS3-ATC	1.946	198.04	1.789×10^{-2}
IMEX3	1.940	0.64	1.775×10^{-2}

Table 6.1: *(Exp. I) EOCs using formula* (6.4) *with $N_1 = 2000$, and $N_2 = 4000$, relative computational times (with STRANG as the reference method) and the L^1 error computed for $N = 2000$.*
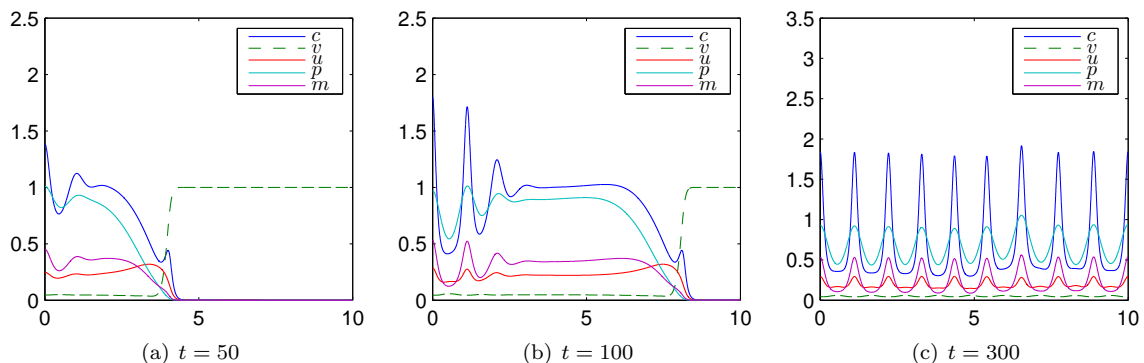

(a) $t = 50$　　　　　(b) $t = 100$　　　　　(c) $t = 300$

Figure 6.4: *(Exp. II) Overview of the dynamics of the system* (3.6) *(over space x) with parameter set $\mathcal{P}$ with $D_c = 5.3 \times 10^{-3}$. A uniform space discretization (cf. Section 5) with 5000 cells and the IMEX3 time integration were employed. The resulting solution is smoother than in Exp. I without exhibiting the same merging/emerging/travelling concentration phenomena.*

6.2 Experiment II

In this experiment we investigate the performance of the methods in the case of a smoother solution. Namely, we consider once again the system (3.6) on the domain $\Omega = (0, 10)$ together with homogeneous Neumann boundary conditions and parameter set $\mathcal{P}$ but choosing an increased diffusion coefficient of the cancer cells, i.e.

$$D_c = 5.3 \times 10^{-3}.$$

Figure 6.4 exhibits the behavior of the solution and comparing to Experiment I, Figure 6.1, we no longer see the dynamic phenomena of merging/emerging, and travelling concentrations; the solution has reached a steady state by $t = 300$.

In order to estimate errors in this setting we make use of a reference solution $\mathbf{w}^{\text{ref}}$, computed with the Dormand and Prince method which we also used to compute the reference solution for Experiment I on $N = 30\,000$ cells. As previously done, we use a fixed Courant number CFL $= 0.49$ and only compute solutions at the fixed time $T = 50$. Test approximations are computed on the domain $\Omega = (0, 5)$ distributed into N uniform cells with
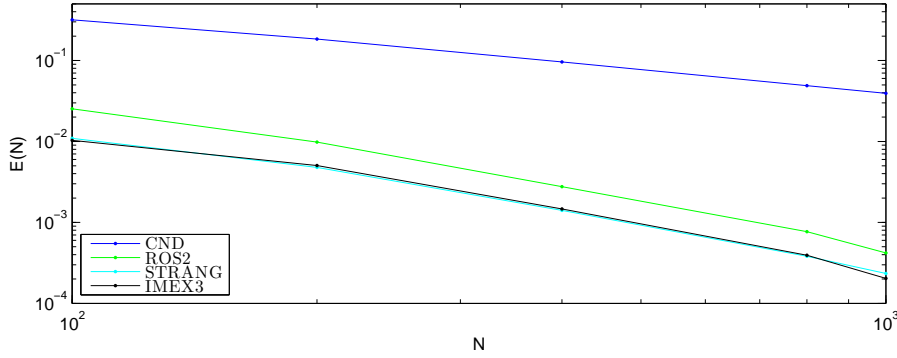
$$N \in \{100,\ 200,\ 400,\ 800,\ 1000\},$$

Figure 6.5: *(Exp. II.) Experimental convergence plot for four selected methods.*

	EOC	discrete L^1 error
CND	0.973	3.933×10^{-2}
ROS2	2.055	4.203×10^{-4}
STRANG	1.958	2.341×10^{-4}
IMEX3	2.154	2.037×10^{-4}

Table 6.2: *(Exp. II) Experimental orders of convergence of four selected methods. The error is computed at the grid $N = 1000$ and the EOC by interpolation between $N_1 = 400$ and $N_2 = 1000$.*

and errors are calculated according to (6.2).

Following the convergence results of Section 6.1 we restrict the study in this section to the most prominent methods STRANG and IMEX3 as well the ROS2 and CND. Figure 6.5 indicates the convergence of these methods. As expected STRANG, ROS2, IMEX3 seem to be second order convergent in space. STRANG and IMEX3 seem to perform best and are almost indistinguishable.

Table 6.2 presents the EOCs –computed according to (6.4)– with $N_1 = 400$ and $N_2 = 1000$. The discrete L^1-error was computed on $N = 1000$ cell grids. Comparing with Experiment I, cf. Table 6.1, we see that the methods exhibit similar EOCs and a significant drop in the actual error, which is due to the smoother solution that their spatial counterpart resolves.

Remark 6.1. In both the larger and smaller diffusion case the STRANG and the IMEX3 methods have produced approximations that are among the most accurate and efficient ones, cf. Sections 6.1, 6.2 and Tables 6.1, 6.2.

6.3 Experiment III

With this experiment we show that the solutions of the reduced system (4.2) equipped with the initial conditions

$$
\begin{cases}
c_0(x) = \exp\left(-\dfrac{x^2}{\varepsilon}\right) \\[2mm]
u_0(x) = \dfrac{1}{2}\exp\left(-\dfrac{x^2}{\varepsilon}\right)
\end{cases}
, \qquad x \in (0, 2), \tag{6.5}
$$

where $\varepsilon = 5 \times 10^{-3}$, and the parameter set (4.3), exhibits also merging and emerging phenomena.

Figure 6.6 shows a graphical representation of the cancer cell concentration c as resolved by the numerical method described in Section 5 with $N = 5000$ uniform computational cells over the domain $\Omega = (0, 2)$; for the time evolution we have employed the STRANG method. As mentioned in Section 4, merging/emerging and travelling concentrations appear in a way very similar to the c component of the system (3.6) when the parameters (3.9) are used, cf. Experiment I in Section 6.1 and Figure 6.1.
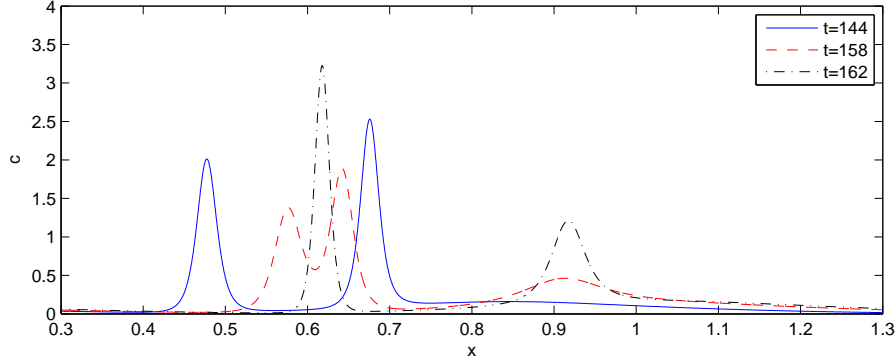
Figure 6.6: *(Exp. III) A focus view of the c component of the reduced system* (4.2). *The spatial distribution for three different time instances shows the merging/emerging/travelling concentration phenomena.*

Due to the small characteristic velocities that appear in practice (in a magnitude of 10^{-2}) the same experiment conducted with the system (4.4) and various $S \in [0, 10^{-2}]$ yields results that are indistinguishable from the solution of the system (4.2).

6.4 Adaptive mesh refinement

Next, we investigate the benefits of adaptive mesh refinement by conducting Experiment I (Section 6.1) again. For our experiments we choose STRANG as time integration method, and the domain $\Omega = (0, 5)$, and set the number of refinement steps $n_{\mathrm{ref}} = 1$, $n_{\mathrm{coa}} = 1$, $n_{\mathrm{ini}} = 3$. Further, we fix the maximum refinement level to be $\mathcal{L}_{\mathrm{max}} = 3$.

We compute the discrete L^1-errors over uniform and non-uniform grids using the formula

$$E(t^n) := |c^{\mathrm{ref},\, \mathrm{n}} - c^n|_{L^1_{\mathrm{disc}}(\Omega)(t^n)} = \sum_{i=1}^{N} \left| C_i^{N_n} \right| \; |c_i^n - c^{\mathrm{ref},\, \mathrm{n}}(x_i)|, \tag{6.6}$$

where $c^{\mathrm{ref},\, \mathrm{n}}$ is the reference solution for the cancer cell density at time t^n, computed by the method of Dormand and Prince on a uniform mesh with 30 000 cells, and c is the the solution obtained by the method whose error we want to compute. Note that the error $E(t^n)$ further depends on the initial number of computational cells N_0.

We consider the absolute gradient of c (5.21) with thresholds $C_{\mathrm{ref}} = 10$, $C_{\mathrm{coa}} = 2.5$, and the estimated discretization error of the characteristic velocities (5.23) with thresholds $C_{\mathrm{ref}} = 2 \times 10^{-5}$, $C_{\mathrm{coa}} = 1.25 \times 10^{-7}$ as monitor functions for the adaptation of the mesh. In the case of the variation monitor (5.22), we adapt the thresholds to the initial grid cell number, i.e. $C_{\mathrm{ref}} = \frac{5}{4N_0}$, $C_{\mathrm{coa}} = \frac{C_{\mathrm{ref}}}{4}$.

Further, we propose a modification of the refinement methods that aims for a better regularized structure of the grid, i.e. we enforce the smoothness condition (5.24) in the following way:

1. If a cell C_i^n which is to be refined has a neighbour C_j^n, $j \in \{i-1,\ i+1\}$ on a lower level $\mathcal{L}_j^n < \mathcal{L}_i^n$, we refine the neighbour C_j^n as well and iterate this strategy with C_j^n.

2. If a cell C_i^n that is marked for coarsening has a neighbour C_j^n on a higher level $\mathcal{L}_j^n > \mathcal{L}_i^n$, which is not marked for coarsening, we do not coarsen C_i^n.

This "smooth refinement" strategy is employed for the following numerical simulations.

Figure 6.7 displays the numerical solution of the system (3.6) with parameters (3.9) over an adaptively redefined grid, using the gradient of c as monitor function and the above mentioned thresholds for the manipulation of the grid. The locality of the grid refinement method is verified by the sizes of the computational cells.
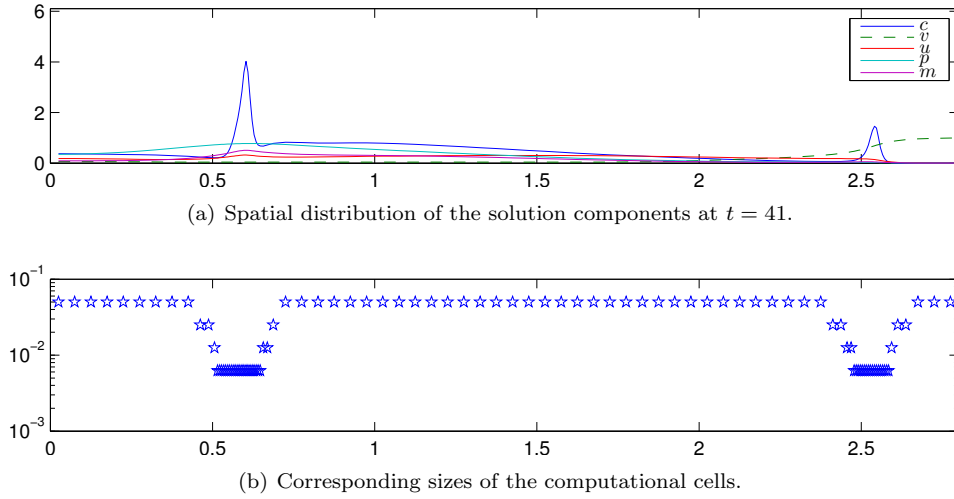
(a) Spatial distribution of the solution components at $t = 41$.

(b) Corresponding sizes of the computational cells.

Figure 6.7: *(AMR-Exp. I) The solution of the system* (3.6), *with parameters and initial conditions as in Experiment I (Sec. 6.1), by employing AMR according to the gradient of c* (5.21), *the thresholds $C_{ref} = 10$, $C_{coa} = 2.5$ and $N_0 = 100$. The size of the computational cells exhibits the (local) refinement of the grid at areas of large gradients of c.*
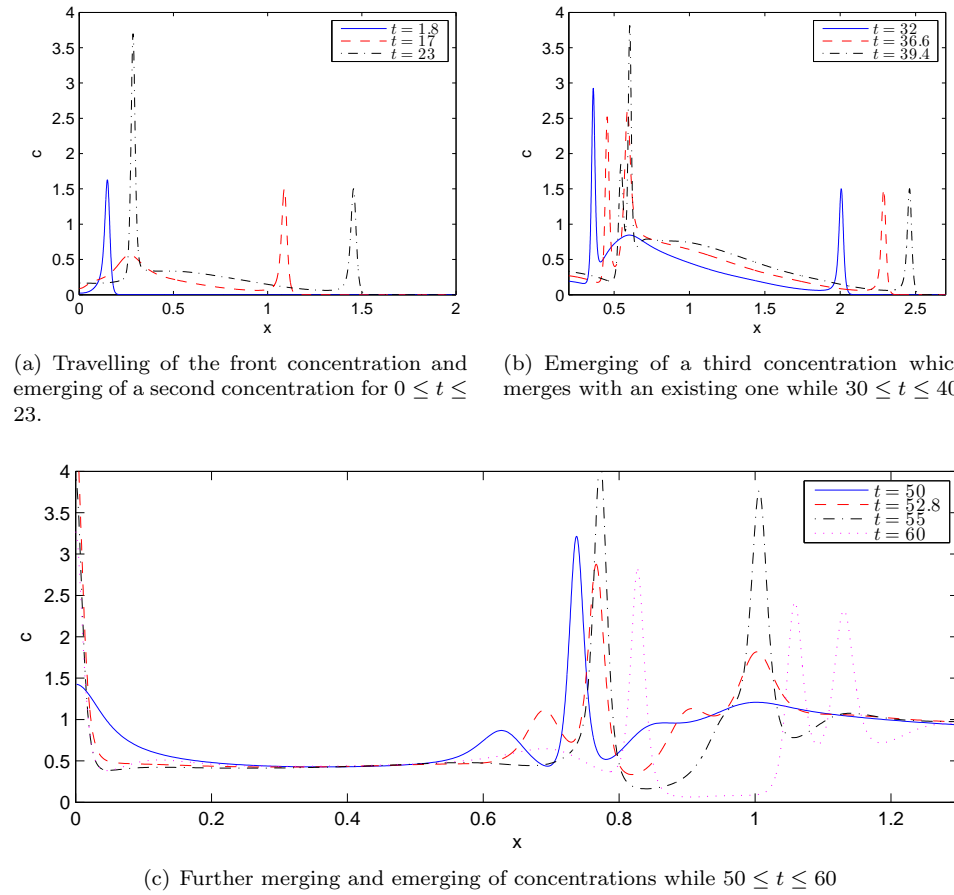

(a) Travelling of the front concentration and emerging of a second concentration for $0 \leq t \leq 23$.

(b) Emerging of a third concentration which merges with an existing one while $30 \leq t \leq 40$.

(c) Further merging and emerging of concentrations while $50 \leq t \leq 60$

Figure 6.8: *(AMR-Exp. I) Dynamics of the cancer cell concentration c for $0 \leq t \leq 60$.*
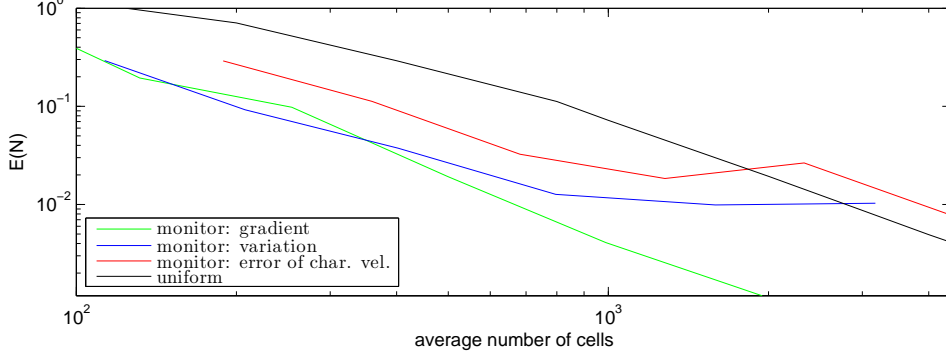
Figure 6.9: *(AMR-Exp. I)Experimental convergence plot of the error* (6.6) *at $t = 50$ for the uniform and three adaptive strategies. Even for higher cell numbers (not showing here), the gradient-based strategy is the most efficient of the four methods.*
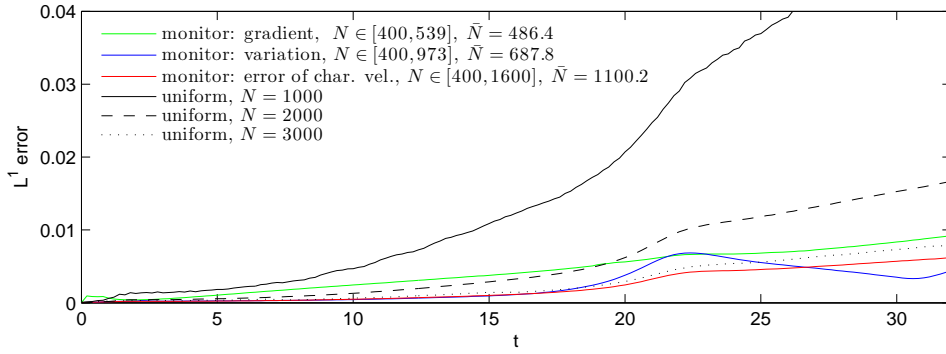

Figure 6.10: *(AMR-Exp. I)Time evolution of the error* (6.6) *for three refinement strategies and three uniform solutions in Experiment I for $t \in [0, 35]$. Showing also the number of computational cells (range and average) that the methods employ. Nonuniform solutions exhibit smaller errors than uniform ones while employing fewer cells.*

Figure 6.8 displays the dynamics of the c component of the solution as they are captured by the adaptive mesh refinement method that we employ (gradient-based monitor function, $N_0 = 1600$ initial grid points, and STRANG time integration). These involve moving, emerging, and merging of concentrations of the cancer cell densities.

Figure 6.9 displays the experimental convergence plots of the discrete L^1-errors (6.6) at $t = 50$, against the average number of cells for the uniform STRANG method and three adaptive strategies. The average cell number of a numerical solution is given by $\bar{N}(t^n) = \frac{1}{t^n} \sum_{k=0}^{n} N_k \tau_k$, where N_k is the total number of computational cell at time t^k. For all adaptive strategies we conducted simulations for $N_0 \in \{50, 100, 200, 400, 800, 1600\}$. For medium/high average-cell-numbers (up to $\bar{N} = 2000$) all three adaptive strategies outperform the uniform, with the gradient-based being the more efficient one. Even on very fine grids, the gradient-based adaptation yields lower errors than the uniform method. Both, the gradient and the error based refinement methods converge in our numerical experiments.

Figure 6.10 shows the time evolution of the error (6.6) for the three adaptive strategies on an initial grid of $N_0 = 400$ cells as well as for various uniform solutions. In the case of the gradient and the variation strategy methods, the error is smaller than the uniform solution on 1000 cells for $t \in [0, 35]$, albeit the refinement methods uses less cells. Employing discretization errors in monitor functions seems to be even more beneficial since the error of the characteristic-velocity based refinement method is during all times $t \leq 35$ less than the error of the uniform solution on 3000 cells. Note that this method uses only 1100 cells in average. The variation based refinement also outperforms the uniform method on 3000 cells except for around $t = 23$, when a second concentration emerges in the solution, cf. Figure 6.8. The error of the gradient based refinement method increases linearly in time and thus does not seem to be affected
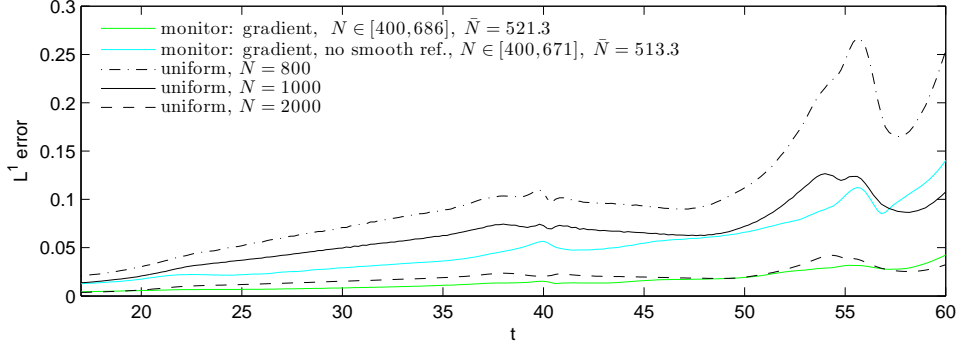
Figure 6.11: *(AMR-Exp. I) Time evolution of the error* (6.6) *of two gradient based refinement methods and three uniform solutions in Experiment I for $t \in [0, 60]$. Showing also the number of computational cells (range and average) that the methods employ. The adaptive gradient strategy method with smooth refinement is significantly more efficient than the adaptive gradient without smooth refinement, while using almost the same amount of grid cells.*

by sudden dynamics of the solution. This way it drops below the error of the uniform method on 2000 cells for $t \geq 20$.

Moreover, Figure 6.11 demonstrates the advantage of the previously introduced smooth refinement strategy, by exhibiting the error evolution of the gradient based refinement method using $N_0 = 400$ with and without smooth refinement during the timespan $t \in [0, 60]$. The smooth refinement method produces solutions close to those on uniform grids with 2000 cells even for large t while the method which does not enforce smoothness condition (5.24) is closer to the uniform solution on 1000 cells. One can further see that employing smooth refinement increases the average number of cells only slightly by 12 and thus does not increase the computational costs significantly. Also the various dynamics of the solution, as e.g. the first process of merging concentrations around $t = 40$, have a smaller impact on the method which employs smooth refinement.

6.5   A 2D experiment

We present results of a 2D-simulation of the system (3.6) which shows similar dynamical phenomena as in the 1D cases.

We have used IMEX3 over $\Omega = [-15, 15]^2$ with uniform discretization with grid size steps $h = (0.05, 0.05)^T$, the parameter set $\mathcal{P}$ (3.9) and the following initial conditions,

$$y(x) = \begin{cases} 4 + 0.7\sin(0.9x), & x < 0, \\ 7\sin(0.9x) + 0.008x^3 + 4, & 0 \leq x \leq 5, \\ 5 + 0.7\sin(4.5) + 0.7\sin(0.9(x-5)), & x > 5, \end{cases}$$

$$\begin{cases} c_0(\mathbf{x}) = \mathbf{1}_{\{x_2 \geq y(x_1)\}}(\mathbf{x}), \\ v_0(\mathbf{x}) = 1 - c_0(\mathbf{x}), \\ u_0(\mathbf{x}) = 0.5c_0(\mathbf{x}), \\ p_0(\mathbf{x}) = 0.05c_0(\mathbf{x}), \\ m_0(\mathbf{x}) = 0, \end{cases} \tag{6.7}$$

for all $\mathbf{x} = (x_1, x_2)^T \in \Omega$. We display results in the window $\bar{\Omega} = [0, 5]^2$, which includes 100×100 grid cells, since this domain stays untouched by reflections, which are caused by the homogeneous Neumann boundary conditions, while $0 \leq t \leq 200$.

The initial conditions and the simulation results are visualized in Figure 6.12. As time evolves the accumulated cancer cells disseminate and degenerate the ECM. They travel in negative x_2 direction,

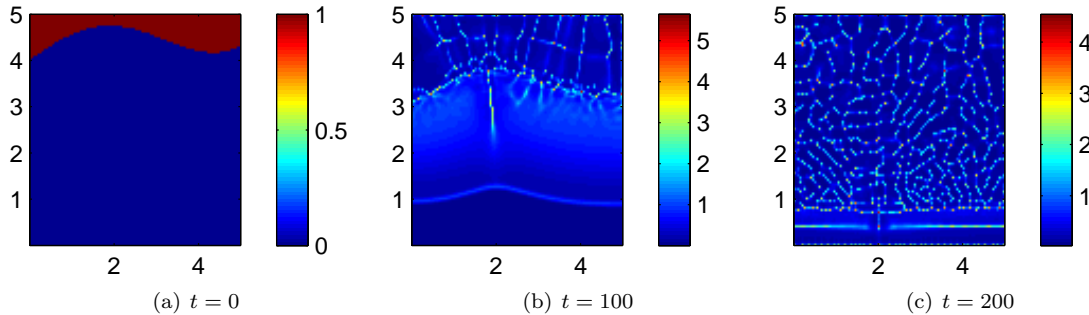(a) $t = 0$ (b) $t = 100$ (c) $t = 200$

Figure 6.12: *(Exp. 2D) Showing here only the cancer cell density c at three time instances.*

towards high densities of vitronectin. Formations of heterogeneous patterns of cancer cells, occurs at areas where the ECM has already degenerated by the propagating cancer cell front. No steady states have appeared until $T = 200$.

Conclusion

We address in this work the formation of cancer cell clusters and the dynamics of cancer cell invasion of the ECM. The model (3.6) that we use, was proposed in [8] and focuses on the role of the serine protease uPA and includes the action of the urokinase-plasminogen-system on the interaction between cancer cells and the ECM, represented by vitronectin.

For such type of systems, a (very) large number of computational cells is needed to resolve the dynamics of the solutions in a consistent way. For smaller cell numbers the numerical approximation errors are of the order of the dynamics or solutions. For that reason, special numerical techniques are deemed necessary.

We describe in Section 5, a higher order finite volume method able to resolve the dynamics of the solution of System (3.6), a wide collection of time integration methods, and the adaptive mesh reconstruction that we employ. Choosing either the STRANG or the IMEX3 method for the time integration we observe, in Section 6, an experimental second order of convergence. STRANG in particular, unlike other methods that have been proposed earlier in the literature for the system (3.6), preserves the positivity of the solution at every time step without requiring local modifications of numerical quantities (see for instance [2]). However, even the high order STRANG method necessitates very fine discretization grids to produce accurate results. To alleviate the computational costs we employ adaptive mesh refinement methods.

In Section 6 we demonstrate the efficiency and accuracy of the mesh refinement technique, in particular of the h-refinement/cell bisection that we employ. We have noticed, with a series of test scenarios, that the best results in terms of errors are obtained if a) the gradient of the cancer cells is used as estimator function for the refinement/coarsening procedure, and b) the grid is smooth (neighbouring cells differ by at most one level of refinement).

Analytically, we have studied in Section 4 a reduced chemotaxis-haptotaxis model with logistic growth (4.2), which we have compared to the original system (3.6) in the following sense: as in the case of the system (3.6) with parameter set $\mathcal{P}$ (3.9), so in the case of the system (4.2), we have found parameters for which the amplification factors of a wide range of Fourier modes are positive. In effect, small perturbations of the steady states of the reaction problem grow with time due to chemotaxis. We have confirmed this behaviour also numerically in Section 6.3, and thus, shown that the system (4.2) exhibits the same phenomena of merging/emerging concentrations. We hence propose it for further development of numerical methods for chemotaxis-haptotaxis cancer invasion models.

Using a saturated chemotaxis system (4.4),(4.5) we have proved L^∞ bounds on the solutions of both systems; this allows us to suggest/propose the smaller model (4.2), and the corresponding parameter set,

as a test case for the further development of mesh refinement techniques for the cancer invasion models. This test case can also be used for the extension of the mesh refinement technique that we have employed here, to the two dimensional case; a task that we will take upon on a subsequent paper.

As noted in the introduction of this work, this is the first in a series of papers where we aim to study different biological theories dealing with the invasion of cancer cells on the ECM under different assumptions on the bio-chemical interaction pathways. In our future study we concentrate on one particular type of cancer and make our cancer-growth model more specific. One application that we have in mind would be the breast cancer, which is of a solid nature and its growth behaviour is quite well-understood and documented. From a numerical point of view, and based on the wellness of the current results, our next steps include the further adaptation of our numerical methods over to 2D domains and the development and analysis of suitable 2D adaptive mesh refinement techniques.

Acknowledgements.

References

[1] W. Alt and D.A. Lauffenburger. Transient behavior of a chemotaxis system modelling certain types of tissue inflammation. *J. Math. Biol.*, 24:691–722, 1987.

[2] V. Andasari, A. Gerisch, G. Lolas, A.P. South, and M.A.J. Chaplain. Mathematical modeling of cancer cell invasion of tissue: biological insight from mathematical analysis and computational simulation. *J. Math. Biol.*, 63:141–171, 2011.

[3] A.R.A. Anderson, M.A.J. Chaplain, E.L. Steele, and R.J.C. Thomson. Mathematical modelling of tumour invasion and metastasis. *Comput. Math. Method. M.*, 2:129–154, 2000.

[4] P. Armitage and R. Doll. The age distribution of cancer and a multi-stage theory of carcinogenesis. *Brit. J. Cancer*, 8:1–12, 1954.

[5] Ch. Arvanitis, Ch. Makridakis, and N. Sfakianakis. Entropy conservative schemes and adaptive mesh selection for hyperbolic conservation laws. *J. Hyperbol. Diff. Eq.*, 2010.

[6] M. Berger, M.J. Aftosmis, and S.M. Murman. Analysis of slope limiters on irregular grids. *AIAA Paper 2005-0490, American Institute for Aeronautics and Astronautics*, May 2005.

[7] K. Boettger, A. Chauviere, H. Hatzikirou, E. Schroeck, B. Klink, and A. Deutsch. Mathematical modelling of cancer growth and treatment. *Springer Lecture Notes in Mathematics Biosciences*, 2013.

[8] M.A.J. Chaplain and G. Lolas. Mathematical modelling of cancer cell invasion of tissue: the role of the urokinase plasminogen activation system. *Math. Models Methods Appl. Sci.*, 15(11):1685–1734, 2005.

[9] A. Chertock, A. Kurganov, X. Wang, and Y. Wu. On a chemotaxis model with saturated chemotactic flux. *Kinet. Relat. Models*, 5(1):51–95, 2012.

[10] E.I. Deryugina and J.P. Quigley. Cell surface remodeling by plasmin: a new function for an old enzyme. *J. Biomed. Biotechnol.*, 2012.

[11] G.P. Dunn, L.J. Old, and R.D. Schreiber. The immunobiology of cancer immunosurveillance and immunoediting. *Immunity*, 21(2):137–148, Aug. 2004.

[12] J.C. Fisher. Multiple-mutation theory of carcinogenesis. *Nature*, 181(4609):651–652, Mar. 1958.

[13] H.B. Frieboes, X. Zheng, C.H. Sun, B. Tromberg, R. Gatenby, and V. Cristini. An integrated computational/experimental model of tumor invasion. *Cancer Res.*, 66(3):1597–1604, Feb. 2006.

[14] A. Gerisch and M.A.J. Chaplain. Robust numerical methods for taxis-diffusion-reaction systems:applications to biomedical problems. *Math. Comput. Modelling*, 43(1-2):49–75, 2006.

[15] A. Gerisch and M.A.J. Chaplain. Mathematical modelling of cancer cell invasion of tissue: Local and non-local models and the effect of adhesion. *J. Theor. Biol.*, 250(4):684–704, 2008.

[16] A. Gerisch and J.G. Verwer. Operator splitting and approximate factorization for taxis-diffusion-reaction models. *Appl. Numer. Math.*, 42(1-3):159–176, 2002.

[17] P.B. Gupta, C.M. Fillmore, G. Jiang, S.D. Shapira, K. Tao, C. Kuperwasser, and E.S. Lander. Stochastic state transitions give rise to phenotypic equilibrium in populations of cancer cells. *Cell*, 146(4):633–644, Aug. 2011.

[18] E. Hairer, S.P. Nørsett, and G. Wanner. *Solving ordinary differential equations. I.* Springer Series in Computational Mathematics. Springer-Verlag, Berlin, second edition, 1993.

[19] T. Hillen, K.J. Painter, and M. Winkler. Convergence of a cancer invasion model to a logistic chemotaxis model. *Math. Models Methods Appl. Sci.*, 2013.

[20] A. Ho and S.F. Dowdy. Regulation of G(1) cell-cycle progression by oncogenes and tumor suppressor genes. *Curr. Opin. Genet. Dev.*, 12(1):47–52, Feb. 2002.

[21] W. Hundsdorfer and J. Verwer. *Numerical solution of time-dependent advection-diffusion-reaction equations.* Springer Series in Computational Mathematics, Springer-Verlag, Berlin, 2003.

[22] J. Katuchova, J. Bober, V. Katuch, and J. Radonak. Significance of lymph node micrometastasis in pancreatic cancer patients. *Eur. Sur. Res.*, 48(1):10–15, Jan. 2012.

[23] C.A. Kennedy and M.H. Carpenter. Additive Runge-Kutta schemes for convection-diffusion-reaction equations. *Appl. Numer. Math.*, 44(1-2):139–181, 2003.

[24] J.F. Kerr, A.H. Wyllie, and A.R. Currie. Apoptosis: a basic biological phenomenon with wide-ranging implications in tissue kinetics. *Brit. J. Cancer*, 26(4):239–257, Aug. 1972.

[25] K. Kessenbrock, V. Plaks, and Z. Werb. Matrix metalloproteinases: regulators of the tumor microenvironment. *Cell*, 2010.

[26] N. Kolbe. Mathematical Modeling and Numerical Simulations of Cancer Invasion. *Master's thesis, Johannes Gutenberg-Universit́at Mainz*, 2013.

[27] D. Kröner and M. Ohlberger. A posteriori error estimates for upwind finite volume schemes for nonlinear conservation laws in multi dimensions. *Math. Comp.*, 69(229):25–39, 2000.

[28] A. Kurganov and M. Lukáčová-Medviďová. Numerical study of two-species chemotaxis models. *Discrete Cont. Dyn-B*, 19(1):131–152, 2014.

[29] O.A. Ladyzenskaja, V.A. Solonnikov, and N.N. Uralceva. *Linear and quasi-linear equations of parabolic type.* AMS, 1968.

[30] G. Lolas. Mathematical modelling of the urokinase plasminogen activation system and its role in cancer invasion of tissue. *PhD thesis, University of Dundee*, 2003.

[31] M. Lukáčová-Medviďová and N. Sfakianakis. Entropy dissipation of moving mesh adaptation. *J. Hyperbol. Diff. Eq.*, 2013.

[32] A. Marciniak-Czochra and M. Ptashnyk. Boundedness of solutions of a haptotaxis model. *Math. Models Methods Appl. Sci.*, 2010.

[33] C.O. Nordling. A new theory on cancer-inducing mechanism. *Brit. J. Cancer*, 7(1):68–72, Mar. 1953.

[34] H. Okada and T.W. Mak. Pathways of apoptotic and non-apoptotic death in tumour cells. *Nat. Rev. Cancer*, 4(8):592–603, Aug. 2004.

[35] K.J. Painter, N.J. Armstrong, and J.A. Sherratt. The impact of adhesion on cellular invasion processes in cancer and development. *J. Theor. Biol.*, 264(3):1057–1067, Jun. 2010.

[36] K.J. Painter and T. Hillen. Spatio-temporal chaos in a chemotaxis model. *Physica D*, 240(4):363–375, 2011.

[37] L. Pareschi and G. Russo. Implicit-Explicit Runge-Kutta schemes and applications to hyperbolic systems with relaxation. *J. Sci. Comput.*, 25(1-2):129–155, 2005.

[38] A.J. Perumpanani, J.A. Sherratt, J. Norbury, and H.M. Byrne. Biological inferences from a mathematical model for malignant invasion. *Invas. Metast.*, pages 209–221, 1996.

[39] N.J. Poplawski, U. Agero, J.S. Gens, M. Swat, J.A. Glazier, and A.R.A. Anderson. Front instabilities and invasiveness of simulated avascular tumors. *Bull. Math. Biol.*, 71(5):1189–1227, Jul. 2009.

[40] L. Preziosi. *Cancer modelling and simulation*. CRC Press, 2003.

[41] G. Puppo and M. Semplice. Numerical entropy and adaptivity for finite volume schemes. *Commun. Comput. Phys.*, 2011.

[42] D. Seiffert, G. Ciambrone, N.V. Wagner, B.R. Binder, and D.J. Loskutoff. The somatomedin b domain of vitronectin. structural requirements for the binding and stabilization of active type 1 plasminogen activator inhibitor. *J. Biol. Chem.*, 1994.

[43] N. Sfakianakis. Adaptive mesh reconstruction for hyperbolic conservation laws with total variation bound. *Math. Comp.*, 2013.

[44] M.B. Sporn. The war on cancer. *Lancet*, 347(9012):1377–1381, May 1996.

[45] T. Stiehl and A. Marciniak-Czochra. Mathematical modeling of leukemogenesis and cancer stem cell dynamics. *Math. Mod. Nat. Phen.*, 7:166–202, 2012.

[46] Z. Szymańska, C.M. Rodrigo, M. Lachowicz, and M.A.J. Chaplain. Mathematical modelling of cancer invasion of tissue: the role and effect of nonlocal interactions. *Math. Models Methods Appl. Sci.*, 2009.

[47] M.C.B. Tan, P.S. Goedegebuure, and T.J. Eberlein. Tumor biology and tumor markers. *Sabiston Textbook of Surgery, The Biological Basis of Modern Surgical Practice*, 18, 2008.

[48] Y. Tao. Global existence of classical solutions to a combined chemotaxis-haptotaxis model with logistic source. *J. Math. Anal. Appl.*, 354(1):60–69, 2009.

[49] Y. Tao and M. Winkler. Energy-type estimates and global solvability in a two-dimensional chemotaxis–haptotaxis model with remodeling of non-diffusible attractant. *J. Diff. Eq.*, 2014.

[50] S. Turner and J.A. Sherratt. Intercellular adhesion and cancer invasion: a discrete simulation using the extended Potts model. *J. Theor. Biol.*, 216(1):85–100, May 2002.

[51] B. Van Leer. Towards the ultimate conservative difference scheme. IV. A new approach to numerical convection. *J. Comput. Phys.*, 23(3):276–299, 1977.

[52] Y. Wei, D.A. Waltz, N. Rao, R.J. Drummond, S. Rosenberg, and H.A. Chapman. Identification of the urokinase receptor as an adhesion receptor for vitronectin. *J. Biol. Chem.*, 1994.

[53] D. Wrzosek. Global attractor for a chemotaxis model with prevention of overcrowding. *Nonlinear Anal.*, 59(8):1293–1310, 2004.

[54] A. Zlotnik. Chemokines and cancer. *Int. J. Cancer*, 119(9):2026–2029, 2006.